Cell Chemical Biology

De novo design of Ras isoform selective binders

Graphical abstract

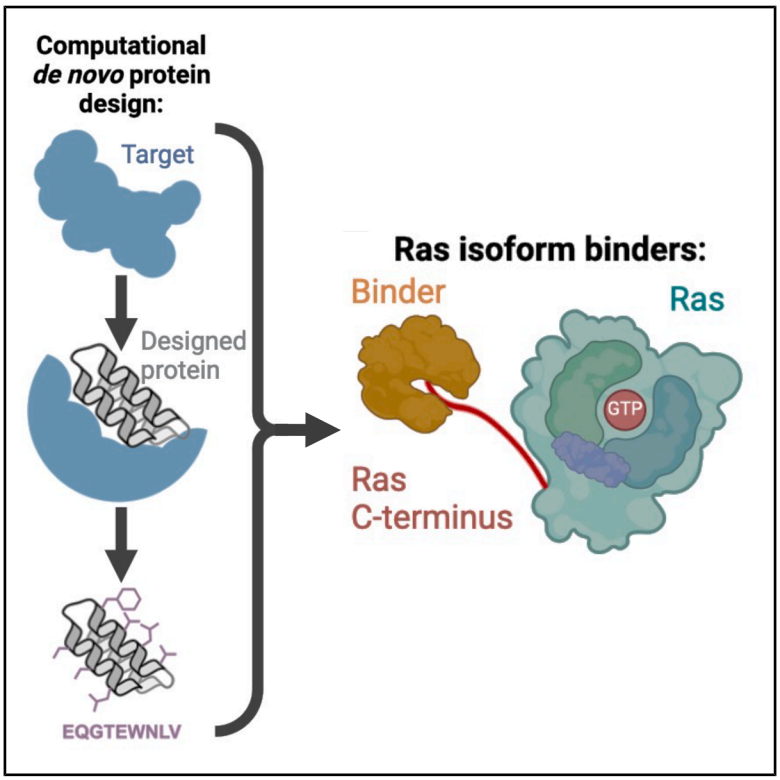

Authors

Jason Z. Zhang, Xinting Li, Alexa Rane Batingana, ..., Benjamin J. Huang, Kejia Wu, David Baker

Correspondence

jzz0428@g.ucla.edu (J.Z.Z.), kejiawu@uw.edu (K.W.), dabaker@uw.edu (D.B.)

In brief

Zhang et al. use deep learning-based protein design to create isoform-specific Ras binders that selectively target the disordered C termini. These tools enable precise dissection of Ras isoform functions and uncover distinct Ras dependencies that emerge during RasG12C inhibitor resistance.

Highlights

- *De novo* protein design yields Ras isoform-specific binders (RIBs)
- RIBs target disordered Ras C termini with high specificity
- RIBs disrupt Ras localization and inhibit signaling in cells
- Isoform-specific tools reveal Ras dependencies during drug resistance

Zhang et al., 2026, Cell Chemical Biology *33*, 1–13
March 19, 2026 Published by Elsevier Ltd.
https://doi.org/10.1016/j.chembiol.2026.02.008

Please cite this article in press as: Zhang et al., *De novo* design of Ras isoform selective binders, Cell Chemical Biology (2026), https://doi.org/10.1016/j.chembiol.2026.02.008

Cell Chemical Biology

CellPress
OPEN ACCESS

Technology

De novo design of Ras isoform selective binders

Jason Z. Zhang,[1,2,3,4,8,10,*] Xinting Li,[1,2] Alexa Rane Batingana,[5] Caixuan Liu,[1,2] Hanlun Jiang,[1,2,6] Kevin Shannon,[5,7] Benjamin J. Huang,[5,7] Kejia Wu,[1,2,8,9,*] and David Baker[1,2,3,9,*]

[1]Department of Biochemistry, University of Washington, Seattle, WA 98195, USA
[2]Institute for Protein Design, University of Washington, Seattle, WA 98195, USA
[3]Howard Hughes Medical Institute, University of Washington, Seattle, WA 98195, USA
[4]Department of Bioengineering, University of California, Los Angeles, Los Angeles, CA 90095, USA
[5]Department of Pediatrics, University of California, San Francisco, San Francisco, CA 94143, USA
[6]Department of Electrical Engineering and Computer Science, University of California, Berkeley, Berkeley, CA 94720, USA
[7]Helen Diller Family Comprehensive Cancer Center, University of California, San Francisco, San Francisco, CA, USA
[8]Biological Physics, Structure and Design Graduate Program, University of Washington, Seattle, WA 98195, USA
[9]These authors contributed equally
[10]Lead contact
*Correspondence: jzz0428@g.ucla.edu (J.Z.Z.), kejiawu@uw.edu (K.W.), dabaker@uw.edu (D.B.)
https://doi.org/10.1016/j.chembiol.2026.02.008

SIGNIFICANCE RAS isoforms play distinct roles in cancer biology, yet their high sequence similarity has made it difficult to study and therapeutically target individual isoforms. This work overcomes a long-standing limitation by using deep learning-based protein design to generate highly specific binders that selectively recognize the otherwise intractable Ras C termini. These isoform-specific binders function *in vitro* and in cells to disrupt membrane localization of Ras and inhibit Ras signaling, enabling precise dissection of isoform-specific functions during drug resistance. Beyond advancing understanding of Ras biology, this study highlights the power of *de novo* protein design as a versatile chemical biology strategy for creating selective tools to probe and potentially modulate complex biological systems.

SUMMARY

The four major isoforms encoded by *RAS* proto-oncogenes are differentially associated with cancer, but there are few isoform-specific binding reagents becasue the sequence differences are confined to their disordered C termini. To overcome this limitation, we use deep learning-based methods to design Ras isoform-specific binders (RIBs) for all major Ras isoforms *de novo* by targeting the Ras C terminus. The RIBs bind to their target Ras isoforms both *in vitro* and in cells with remarkable specificity, disrupting their membrane localization and inhibiting Ras activity. The RIBs enable dissection of the distinct roles of Ras isoforms during Ras^{G12C} inhibitor resistance, demonstrating their utility in understanding Ras biology and disease and suggesting potential therapeutic applications.

INTRODUCTION

The Ras family of GTPases modulates mitogen-activated protein kinase (MAPK) and other intracellular signaling pathways essential for cell growth and survival, and *RAS* mutations are highly prevalent in many human cancers. The four major Ras isoforms—KRAS4A, KRAS4B, HRAS, and NRAS—have high sequence homology and similar biochemical properties. Despite their similarities, *RAS* genes are differentially mutated in cancer,[1] play different roles in drug resistance,[2] and have distinct subcellular locations[3,4] due to their divergent disordered and highly charged C termini. Whereas the structured portion of all Ras isoforms share 90% sequence identity, the sequence identity over the C termini is only 8% (Figures 1A and 1B). While all isoforms can localize to the plasma membrane (PM), NRAS, HRAS, and KRas4A are reversibly palmitoylated on their hypervariable C termini, enabling endomembrane localization and rapid trafficking between different cell compartments.[3,4] It has been challenging to develop Ras isoform-specific reagents[5,6]; those that are available often detect multiple bands in immunoblotting experiments and are insufficient for more sensitive assays such as immunostaining. Despite decades of research into the different Ras isoforms, their specific signaling activities and functional roles remain unclear due to the lack of isoform-selective molecular tools, such as selective affinity reagents, complicating precise functional studies.

Please cite this article in press as: Zhang et al., *De novo* design of Ras isoform selective binders, Cell Chemical Biology (2026), https://doi.org/10.1016/j.chembiol.2026.02.008

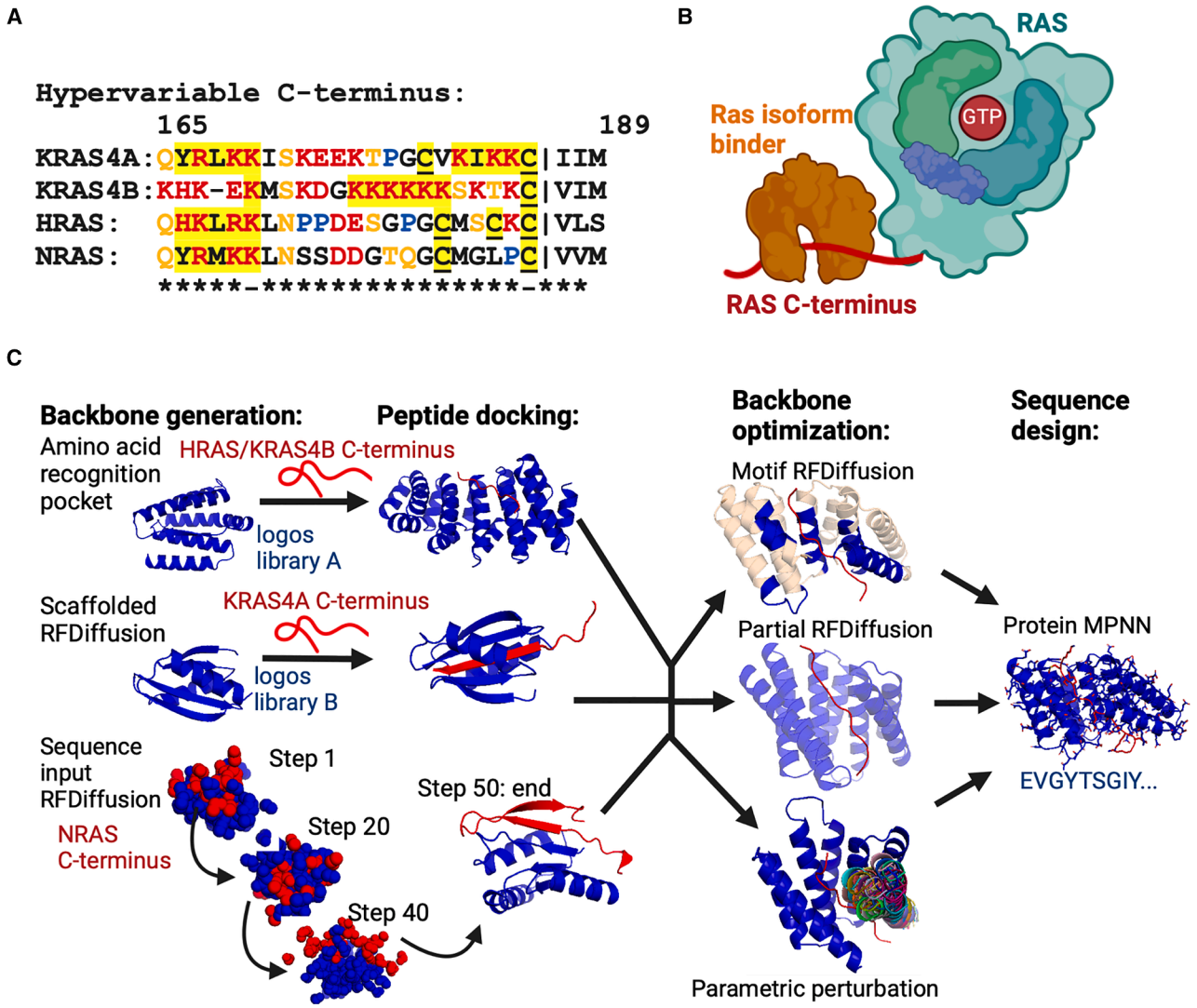

Figure 1. Computational design methods

(A) Sequence alignment of the C termini of the major Ras isoforms. Residues in red are charged, in orange are polar, and in blue are prolines. Highlighted in yellow are residues involved in membrane interaction. Underlined residues undergo lipid modification.

(B) Schematic representation of RIBs binding to the Ras C terminus.

(C) Computational design. Backbone generation either through an amino acid recognition pocket-based approach, scaffolded RFDiffusion, or sequence input diffusion. These peptide-scaffold backbones are then optimized through motif RFDiffusion (subsets of the backbone kept fixed), partial RFDiffusion (slightly altering the overall scaffold backbone), or parametric perturbation (rotating/moving a portion of the scaffold backbone in a specified manner). Next, ProteinMPNN was used to optimize the amino acid sequence for a given scaffold backbone. Scaffold-target complexes are evaluated using AlphaFold2 and Rosetta metrics to determine what to experimentally characterize.

Recent advances in protein design[7–9] now enable the design of binders to a wide range of protein targets. Our goal was to design Ras isoform-specific binders (RIBs) by targeting the disordered and highly charged C terminus of Ras (Figure 1A) as it is the only region that significantly differs between the Ras isoforms. Targeting highly polar, native protein regions such as these C termini of Ras (e.g., KRAS4B C terminus is 86% polar residues, 63% charged residues) has been difficult[10] due to the biochemical challenge of binder interactions competing with water. Precise and extensive polar interactions are required to develop Ras binders that avoid the substantial enthalpic penalty for stripping away water-mediated hydrogen bonds and entropic penalty for stabilizing intrinsically disordered C terminus of Ras. We reasoned that recently developed methods for designing binders to intrinsically disordered regions[11,12] could enable the design of RIBs superior to currently available antibodies. These reagents might also provide valuable tools for dissecting the roles of the different isoforms in cellular function and disease and could provide scaffolds for developing isoform-selective chemical inhibitors, demonstrating the overall value of protein design in creating chemical biology tools for understanding cell biology.

Please cite this article in press as: Zhang et al., *De novo* design of Ras isoform selective binders, Cell Chemical Biology (2026), https://doi.org/10.1016/j.chembiol.2026.02.008

DESIGN

To enable true isoform selectivity without perturbing the conserved catalytic core of Ras, we sought to design binders that recognize sequence-encoded chemical features unique to each hypervariable C terminus rather than relying on structural mimicry of pre-existing Ras-binding scaffolds. We aimed to create small, stable proteins capable of engaging highly charged, conformationally flexible peptides with sufficient interaction density to discriminate among closely related sequences and also binding full-length Ras in cells. We based our approach on three design principles: (1) maximize sequence discrimination by encoding networks of side-chain-specific hydrogen bonds and electrostatic interactions distributed across the divergent C-terminal residues, (2) allow structural plasticity during backbone generation to accommodate targets that may adopt induced conformations upon binding, and (3) incorporate stringent *in silico* stability and interface quality filters to enrich for compact, expressible scaffolds suitable for high-throughput screening. Multiple backbone-generation campaigns were evaluated to determine whether target stabilization through β sheet formation or extended recognition would better support specificity, and refinement strategies were implemented to reduce steric incompatibility with full-length Ras while preserving critical polar contacts. Lipid modifications and membrane context were not explicitly modeled during initial generation to maintain tractability and generalizability of the pipeline; instead, compatibility with full-length and modified Ras proteins was addressed through iterative refinement and downstream validation.

RESULTS

Computational design of Ras isoform-selective binders

We explored two different peptide binder strategies for designing RIBs. The first "side-chain-centered" approach threads the sequences of disordered regions (intrinsically disordered regions [IDRs]) through ∼800 protein templates from logos[11] (logos library A) with specific amino acid recognition pockets arranged to bind diverse sequences in a range of extended conformations. The second "backbone-centered" strategy generates backbones via either "scaffolded RFDiffusion" by threading the sequences into a subset of ∼200 β sheet-containing wrapping-up scaffolds also from logos[11] (logos library B) or from random noise using sequence input RFdiffusion[12] in which both the backbone conformation of the binder and the target were widely sampled. In both cases, the top scored designs are optimized by the "refinement" protocol from the standard logos pipeline,[11] i.e., partial RFDiffusion,[13] motif RFDiffusion,[11] and parametric perturbation.[14] Sequences are all designed using ProteinMPNN.[8] Designs are selected for experimental characterization based on AlphaFold 2 (AF2)[15] prediction confidence metrics (pae interaction), predicted binding affinity (Rosetta ΔΔG), and extent of buried polar atoms without hydrogen binding (buried unsaturated residues)[11] (Figure S1). To achieve specificity, we prioritized binders with extensive polar interactions with the Ras C terminus but disregarded the last 4 residues, which get cleaved and then undergo farnesylation.

Initially, we attempted to design binders to all Ras isoforms using all methods. We found that both scaffolded and sequence input RFDiffusion methods primarily produced binder backbones that induced the target to conform to regular secondary structures. This worked well with the KRAS4A and NRAS C termini, which were induced to form β strands that formed an extended β sheet with the binder, but not for the KRAS4B and HRAS C termini, which are less compatible with regular secondary structure (KRAS4B has a highly charged 6× lysine region, and HRAS contains several unevenly spaced proline residues). The amino acid recognition pocket-based approach was more successful in generating good scoring designs for all the Ras isoforms as it does not require any secondary structure propensity in the target. We selected for experimental characterization 8,317 (5,254 from sequence input and 3,063 from scaffolded) and 3,078 (343 from sequence input and 2,735 from scaffolded) designs made using RFDiffusion for KRAS4A and NRAS, and 2,556 and 1,264 designs made using the amino acid recognition pocket-based approach for KRAS4B and HRAS.

In vitro testing of *de novo*-designed RIBs

We obtained synthetic DNA encoding the selected RIB designs and identified binders using yeast display[16,17] (see STAR Methods for details, Figures S2A and S2B). For KRAS4B and NRAS, the initial RIB library showed specific binding to the C terminus but did not bind to full-length Ras, perhaps due to steric interference with the full-length proteins, which were not considered in our original design calculations. We carried out a second round of binder scaffold optimization via motif and partial RFDiffusion requiring compatibility with both the C terminus and full-length protein (Figure S2C), which resulted in smaller scaffolds clashing less with the target. For example, the helix of the KRAS4B C-terminal binder is predicted to clash with a portion of the structured domain of KRAS4B, and hence portions of that helix were re-designed to accommodate binding for full-length KRAS4B (Figure S2D). Ultimately, yeast display selection yielded ∼250 binders for KRAS4A, ∼90 binders for NRAS, ∼50 binders for HRAS, and ∼20 binders for KRAS4B. Of note, while designs with diverse structural folds were ordered, the successful binders had relatively similar folds for the same target, possibly hinting that the Ras C termini have a preferred conformation (Figure S3A; Table S1). For KRAS4A, binders were obtained from scaffolded RFDiffusion where a portion of the KRAS4A C terminus adopts a β strand conformation, which forms extended β sheet hydrogen bonds with the binder's β sheet (Figures 2A and S3A). In contrast, NRAS binders came from sequence input RFDiffusion and induced NRAS to adopt a conserved conformation where it formed multiple β strands to create extended β sheets with the binder (Figures 2A and S3A). The successful KRAS4B and HRAS binders came from the amino acid recognition pocket approach and induced KRAS4B or HRAS to adopt a non-regular secondary structure with an extended interface (Figures 2A and S3A).

We next expressed and purified the top 10 RIB hits from yeast display per target for *in vitro* characterization. Corroborating the yeast display results, RIBs specifically bound to their cognate full-length target (Figure 2B) with affinities ranging from 35 to 1,300 nM (Figures S3B and S3C; Table S1) measured using bilayer interferometry. The RIBs bound to their intended target in a nucleotide and prenylation-independent manner. These

Please cite this article in press as: Zhang et al., *De novo* design of Ras isoform selective binders, Cell Chemical Biology (2026), https://doi.org/10.1016/j.chembiol.2026.02.008

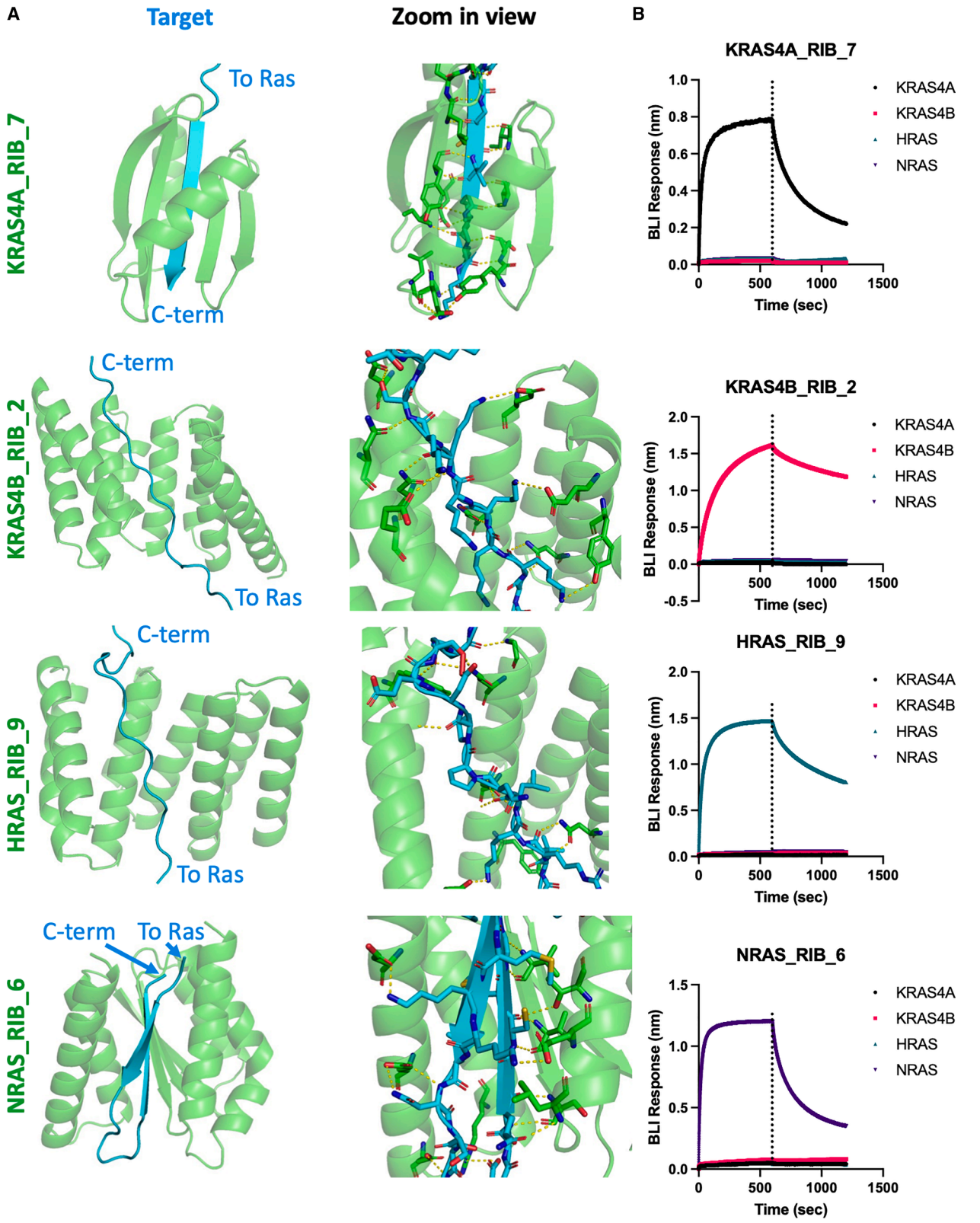

(legend on next page)

Please cite this article in press as: Zhang et al., *De novo* design of Ras isoform selective binders, Cell Chemical Biology (2026), https://doi.org/10.1016/j.chembiol.2026.02.008

results were expected as the C terminus of Ras is distal from the nucleotide-binding site[1] in the structured portion (Figure S3D), and we designed our binders to not bind to the last 4 amino acids. We independently verified that our RIBs bind to the prenylated form of each RAS isoform *in vitro* (Figure S3E). All 10 RIBs (numbered based on biolayer interferometry [BLI]-derived K_D ranking) for each target that were tested experimentally bound both *in vitro* and in cell experiments (Table S1), and the RIBs with the most consistent and specific binding throughout the experiments are shown in Figure 2, sequences are listed in Table S2, and are used for the rest of the paper (Figures 3, 4, and S5–S7). Of note, the binders with tight affinity (K_D < 100 nM, Table S1) were not necessarily the most specific when applied in cell experiments. In the design model of the scaffolded RFDiffusion-generated KRAS4A_RIB_7:KRAS4A complex, the C-terminal section of the KRAS4A C terminus forms a β strand that pairs with β strands deep within the binder and is packed by surrounding helices. In the design model of the sequence input RFDiffusion-generated NRAS_RIB_6:NRAS complex, the NRAS C terminus forms two β strands (innermost β strand is NRAS C terminus), which is incorporated into an extended β sheet with the binder and is packed by surrounding helices. In the design model of the amino acid recognition pocket-derived KRAS4B_RIB_2:KRAS4B and HRAS_RIB_9:HRAS complex, a portion of the KRAS4B or HRAS C terminus forms an extended unstructured interface with the binder. Further characterization of KRAS4B_RIB_2 demonstrates this binder's specificity as it does not bind to similar polylysine regions such as those in RAC1,[18] does not bind to KRAS4B C terminus added to other proteins, but can still bind to the Serine 181-phosphorylated KRAS4B C terminus[19] (Figures S3F–S3H). We also tested whether our RIBs preferentially bound to the palmitoylated or non-palmitoylated version of KRAS4A, HRAS, or NRAS (KRAS4B does not undergo palmitoylation). BLI experiments demonstrate that KRAS4A and NRAS RIBs do not bind to palmitoylated versions of their target, while HRAS RIB binds to de-palmitoylated HRAS C terminus (Figure S3I). These data align with their design models as the predicted binding interface for KRAS4A and NRAS RIBs includes that palmitoylated cysteine but not for the HRAS RIB.

RIBs identify RAS isoforms in mammalian cells

To test the ability of RIBs to selectively bind Ras isoforms in mammalian cells, we used "Ras-less" mouse embryonic fibroblast cell lines (MEFs) that express a single wild-type (WT) Ras[20,21] isoform (e.g., KRAS4A Ras-less MEFs express only WT KRAS4A). To test for RIB specificity, we carried out the analog of an immunoblot in which Ras-less MEF cell lysates separated on SDS gels were probed with biotinylated RIBs followed by labeling by Alexa Fluor 488-conjugated streptavidin (see STAR Methods for details). For each RIB, little binding was observed for the non-cognate cell lines, and a single band with the molecular weight of Ras was observed in the cognate cell line (Figure 3A). To determine whether RIBs can detect endogenous levels of the target, we carried out small interfering RNA (siRNA) knockdown experiments in unmodified WT MEFs that express all the major Ras isoforms (Figure 3B). These siRNAs were validated in previous reports and are listed in the STAR Methods. RIB-mediated band signal was lost only when its target was knocked down (e.g., only NRAS siRNA eliminates NRAS RIB-mediated band). To test whether RIBs can detect endogenous levels of Ras isoforms, we probed WT MEFs and observed only one major band was seen around 20 kDa, the expected molecular weight of Ras (21 kDa) (Figure 3C). In contrast, the most specific known Ras isoform antibodies[5] displayed many non-specific bands across a variety of cell lines (Figure S4), demonstrating that the specificity of RIBs compares favorably to available antibody reagents.

Imaging Ras isoforms in cells

We investigated whether the RIBs are sufficiently specific and sensitive for fluorescence imaging assays by applying biotinylated RIBs to fixed and permeabilized Ras-less MEFs and used Alexa Fluor 488-conjugated streptavidin for imaging detection. The RIBs only stain their respective Ras-less MEFs (e.g., KRAS4A RIB fluorescence signal is only seen in KRAS4A Ras-less MEFs), with no significant signal in the other Ras-less MEFs (Figures 3D and S5A). As reported in previous studies,[5] only a subset of cells showed significant staining signal possibly due to heterogeneity in Ras isoform expression. RIB staining largely aligns with known subcellular localization[4,22] of Ras isoforms as well: KRAS4A RIB staining co-localized with PM and mitochondria, KRAS4B RIB staining co-localized with PM, and HRAS and NRAS RIB staining co-localized with PM and Golgi, with NRAS RIB having the most co-localization with Golgi and the least co-localization with PM (Figure S5B). The specific fluorescence labeling with the RIBs is greater than that of the previously described isoform-specific antibodies,[5] which do not show significant immunostaining signal in the corresponding Ras-less MEF cell line (Figure S5C). Only the NRAS antibody showed significant immunostaining signal, but knockdown of NRAS via siRNA did not diminish immunostaining signal, suggesting lack of specificity (Figure S5B).

The fluorescence staining results suggested differences in localization with KRAS4B having the most PM localization and NRAS the most endomembrane signal, consistent with previous work.[2,3] However, localization using the RIBs could be biased if RIB binding is reduced by Ras C-terminal palmitoylation (Figure S3I) since we did not include covalent modification by palmitoylation in our initial design computations. This aligns with our predicted complex structures of NRAS RIB with NRAS C terminus, which shows that the NRAS palmitoylation site C181[3,23,24] is buried within the interface. Accordingly, we hypothesized that the lower signal co-localization of NRAS at PM could be due to the NRAS RIBs binding primarily to the non-palmitoylated version of NRAS, which should be more endomembrane localized. Ras-less MEFs that proliferate due to

Figure 2. RIBs specifically bind to their target *in vitro*

(A) Design models of the RIBs (green) in complex with their Ras C-terminal targets (cyan). Dotted yellow lines represent polar interactions between binder and target.

(B) Representative biolayer interferometry (BLI) results of RIBs (1 μM) interacting with the full-length proteins of different Ras isoforms. In each case, binding is specific for the intended target. Each experiment was repeated 3 times.

Please cite this article in press as: Zhang et al., *De novo* design of Ras isoform selective binders, Cell Chemical Biology (2026), https://doi.org/10.1016/j.chembiol.2026.02.008

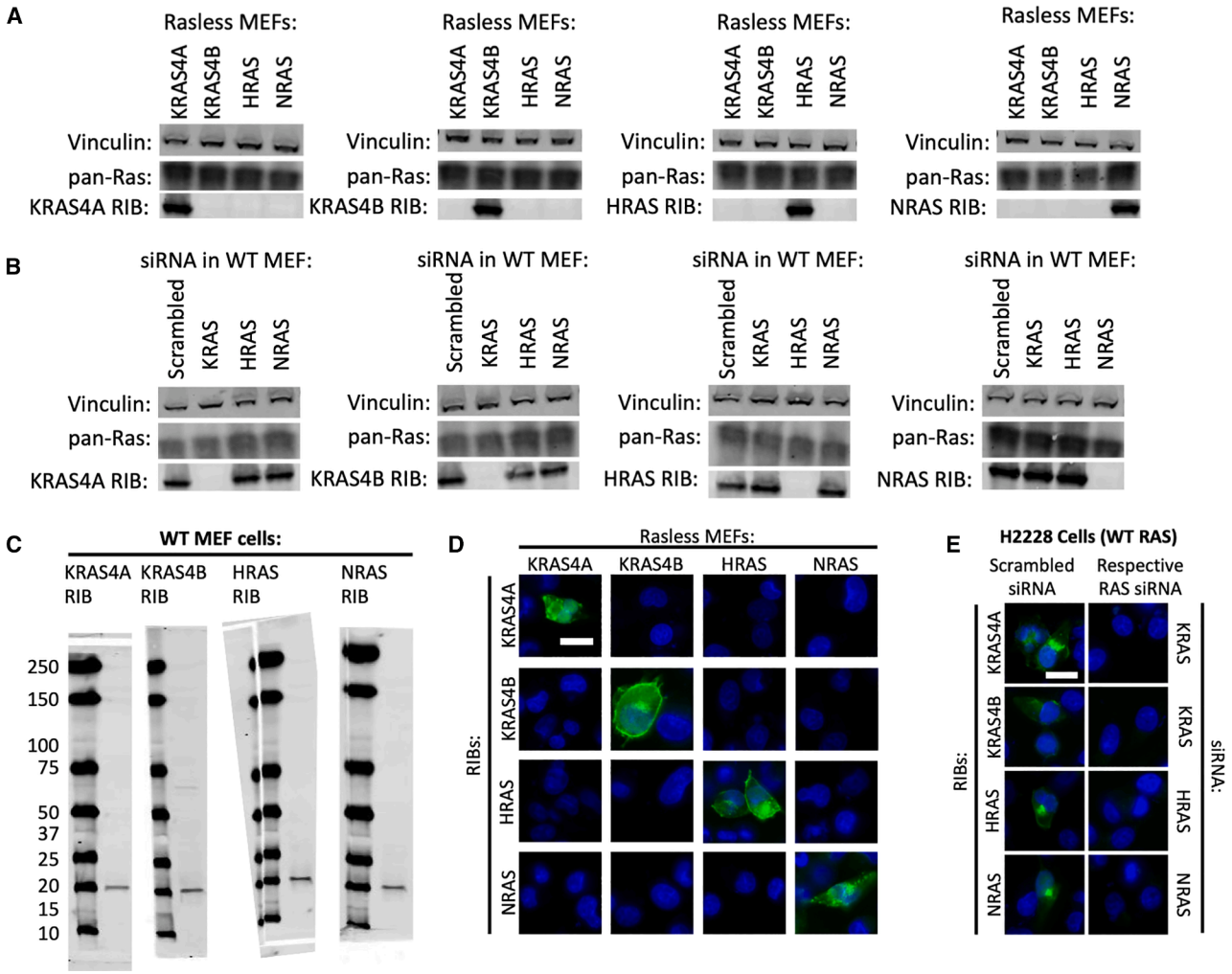

Figure 3. RIBs specifically bind to their targets in cells

(A) Lysates from Ras-less MEFs, which express only one WT Ras isoform at a time, were run on SDS-PAGE gels, and the Ras isoforms were probed with 10 μM biotinylated RIBs or antibodies. Shown are representative blots from 3 independent experiments.

(B) Wild-type (WT) MEF cells were transfected with either Scrambled or Ras isoform-specific siRNA. Two days later, cells were lysed, ran on SDS-PAGE gels, and probed with biotinylated RIBs or other antibodies. Shown are representative blots from 3 independent experiments.

(C) WT MEF lysates were run on SDS-PAGE gels and probed with biotinylated RIBs. Shown are representative full blots from 6 independent experiments.

(D) Ras-less MEFs were probed via biotinylated RIBs (green) and DAPI (blue). Shown are representative epifluorescence images from 3 independent experiments. Scale bars, 10 μm.

(E) WT H2228 cells were transfected with either Scrambled or Ras isoform-specific siRNA. Two days later, cells were fixed, permeabilized, and probed with biotinylated RIBs (green) and DAPI (blue). Shown are representative epifluorescence images from 3 independent experiments. Scale bars, 10 μm.

exogenous BRAF V600E expression lack all four Ras isoforms. Ectopically expressing NRAS WT or palmitoylation-resistant C181S, NRAS RIBs in these cells pulled down NRAS C181S[3,23,24] to a greater extent than NRAS WT (Figure S6), suggesting that NRAS RIBs preferentially bind to the non-palmitoylated forms of NRAS.

To assess if our RIBs can label endogenous levels of Ras isoforms in intact cells, H2228 cells that contain all major Ras isoforms were transfected with Ras isoform-selective siRNAs. While each of the RIBs had detectable staining signal when scrambled siRNA was transfected, knockdown of the targeted Ras isoform in H2228 cells eliminated this signal (Figure 3E), demonstrating that RIBs can measure endogenous Ras isoforms. This has not been achievable with previously described isoform-specific antibodies.[5]

Overexpression of RIBs disrupts Ras localization and signaling

We next explored the effects of ectopically expressing individual RIBs in cells. As the C-terminal hypervariable domains of Ras proteins regulate trafficking and membrane localization, we reasoned that RIBs might disrupt these processes. In Ras-less MEFs that express one isoform, the corresponding RIB shifts the Ras isoform from being in the membrane to the cytosolic

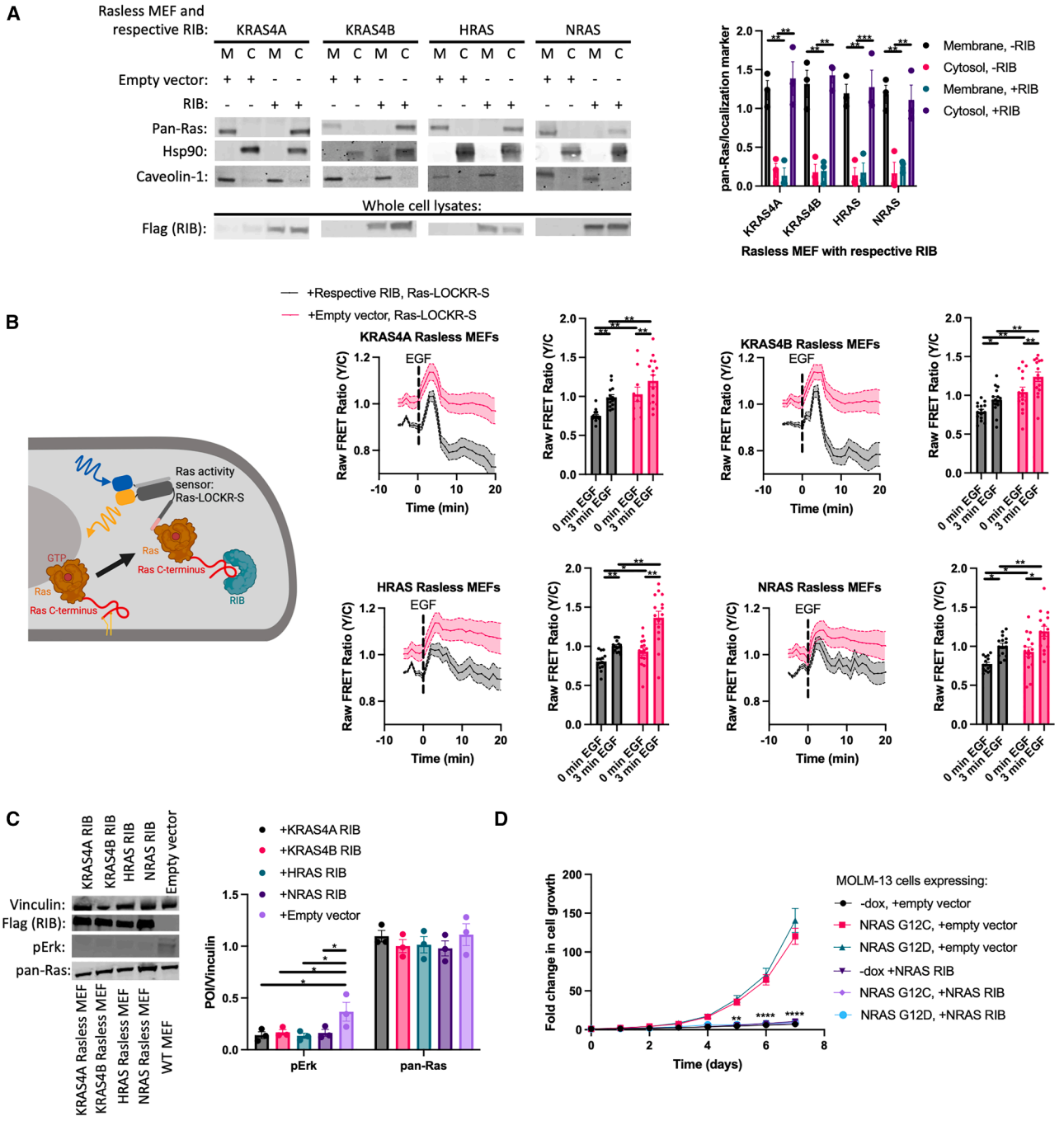

Figure 4. RIB expression alters Ras localization and signaling

(A) Ras-less MEFs were transfected with either empty vector (−RIB) or their respective RIB (+RIB) for 1 day, lysed, and underwent membrane fractionation and immunoblotting analysis (see STAR Methods for details). Left: representative immunoblot. On the top are different cell fractionations (membrane, M vs. cytosol, C). On the bottom is whole-cell lysates. Right: densitometry quantification of immunoblots comparing pan-Ras signal with the signal from the localization marker (Hsp90 for cytosol and Caveolin-1 for membrane) (n = 3 experiments). Statistics: two-way ordinary ANOVA. p values (from left to right): 0.0059, 0.0074, 0.0023, 0.0057, 0.0082, 0.00042, 0.0027, and 0.0044.

(B) Ras-less MEFs were transfected with Ras-LOCKR-S and either RIB fused to mCherry or empty vector. Then cells were imaged and stimulated with 100 ng/mL epidermal growth factor (EGF). Top left: schematic of experiment. Left: time-course imaging of raw FRET ratios (yellow over cyan [Y/C]) representative of three independent experiments. Right: bar graph quantification of the Ras-LOCKR-S raw FRET ratios across all experiments (n = 15 cells per experiment). Statistics: two-way ordinary ANOVA. p values (from left to right, top to down): 0.0047, 0.0029, 0.0091, 0.0082, 0.017, 0.0082, 0.0095, 0.0041, 0.007, 0.023, 0.0048, 0.0042, 0.034, 0.044, 0.0052, and 0.032.

(legend continued on next page)

Please cite this article in press as: Zhang et al., *De novo* design of Ras isoform selective binders, Cell Chemical Biology (2026), https://doi.org/10.1016/j.chembiol.2026.02.008

fraction (Figure 4A, see STAR Methods for details of fractionation), suggesting that RIB overexpression disrupts Ras membrane localization.

The canonical view is that Ras requires a membrane to be in its active GTP-loaded state,[1,27,28] but a membrane-less cytosolic pool of Ras[24,29] could also be active. As RIB expression enhances the cytosolic localization of Ras, we explored whether this perturbation in Ras localization alters activation and signaling. We used a previously constructed Ras activity biosensor (Ras-LOCKR-S[27]) to measure Ras-GTP loading in live cells with single-cell resolution. Ras-less MEFs expressing either mCherry-tagged RIB or empty vector and co-expressing untargeted Ras-LOCKR-S to measure whole-cell Ras activity were imaged (Figure 4B). For all the Ras isoforms tested, the Ras-LOCKR-S FRET ratios (yellow over cyan [Y/C]), which report on Ras-GTP loading, were lower in cells overexpressing RIBs ("0 min EGF" in Figure 4B). However, upstream Ras activation by stimulation with 100 ng/mL epidermal growth factor (EGF) still induced some transient Ras activation ("3 min EGF" in Figure 4B) when RIBs were expressed, and this is true for all Ras isoforms tested. While KRAS4A and KRAS4B Ras-less MEFs displayed transient activation of Ras with Ras signaling returning to baseline or lower levels, NRAS and HRAS Ras-less MEFs showed transient Ras activation where Ras activity persists 10 min after EGF stimulation[30] (Figure 4B). These differences in Ras activity dynamics may be due to the differential localization of these Ras isoforms. A negative control (NC) version of Ras-LOCKR-S[27] that is a point mutant away from Ras-LOCKR-S but renders the biosensor insensitive to Ras-GTP displayed no difference in FRET ratios between RIB and empty vector expression (Figure S7A).

We measured phosphorylated Erk (pErk) levels in Ras-less MEFs to assess the effects of RIB expression on MAPK pathway activation. Ras-less MEFs expressing their respective RIBs displayed decreased pErk/vinculin levels compared to WT MEFs transfected with empty vector (Figure 4C). However, EGF stimulation in these same conditions led to increases in pErk/vinculin levels that were indistinguishable from WT MEFs transfected with empty vector (Figure S7B), corroborating our Ras-LOCKR-S data showing that Ras activity can still be stimulated when RIBs are expressed. This Erk activation observed in the presence of RIBs is dependent on Ras farnesylation as dual farnesyl transferase and geranylgeranyl transferase-1 inhibition greatly diminishes pErk levels (Figure S7C), aligning with previous reports indicating that Ras activation and downstream signaling require farnesylation.[31] As the last 3 C-terminal residues, which get cleaved after farnesylated and cleaved, were not included in RIB design, we expect that RIB binding to Ras isoforms is not influenced by farnesylation. Probing with a pan-Ras antibody showed no significant differences in Ras levels (Figures 4C and S7B), suggesting that these decreases in basal pErk/vinculin levels are not due to Ras protein expression differences. To verify that RIB overexpression only affects their respective Ras isoform, RIBs were overexpressed in all the Ras-less MEFs and probed for Ras activity levels via Ras-LOCKR-S or Erk activation via pErk/Erk levels (Figure S7D). Only RIB expression in their respective Ras-less MEF decreased Ras activity and Erk activation, demonstrating the specificity of the designs. Overall, these results corroborate the dogma that Ras-GTP loading is enhanced when in proximity to membranes but also suggest that cytosolic Ras can be activated and lead to downstream signaling.

As RIBs can disrupt Ras localization and signaling, we wondered if RIB expression might alter cell proliferation. We focused on NRAS as our NRAS RIBs have a clear preference for non-palmitoylated NRAS (Figure S6), which aligns with *in vitro* binding data (Figure S3I). NRAS depalmitoylation has emerged as a promising therapeutic strategy for melanoma, hematologic cancers, and other *NRAS*-mutant cancers.[32,33] We expressed NRAS RIB in engineered isogenic MOLM-13 cell lines that are dependent on doxycycline-induced expression of mutant NRAS or KRAS4B. We found that NRAS RIB inhibited the growth of mutant NRAS-dependent MOLM-13 cell lines (Figure 4D) but not KRAS4B-expressing MOLM-13 cells or MOLM-13 cells not exposed to doxycycline to induce RAS protein expression (Figures 4D and S8). These results indicate that perturbing the localization of Ras can influence Ras activation, downstream signaling, and cell growth.

Utility of RIB to understand the Ras isoform functions during Ras^{G12C} inhibition

Based on the above data indicating that RIBs might function as Ras isoform-selective inhibitors, we sought to use them to probe the function of individual Ras isoforms during Ras^{G12C} inhibition. *KRAS*^{G12C} mutations are prevalent in lung adenocarcinoma, and tumors that recur after an initial response to small molecule inhibitors such as sotorasib reactivate the oncogenic Ras signaling. A previous report showed that Golgi-localized Ras activity is important for downstream MAPK signaling and cell growth while mitochondria-localized Ras activity alters metabolic flux. However, the Ras isoform(s) that mediate these segregated Ras activities and functions during Ras^{G12C} inhibition are unclear.

We used the RIBs to inhibit one Ras isoform at a time in the presence or absence of sotorasib and measured the resultant subcellular Ras signaling with a subcellularly localized Ras-LOCKR-S (Figure 5A). In the absence of RIBs, Ras activity time courses differ across the subcellular region in *KRAS*^{G12C}-mutant MIA PaCa-2 pancreatic cancer cells. At the PM, Ras signaling measured by PM-localized Ras-LOCKR-S starts off as relatively high, rapidly decreases within 4 h of sotorasib treatment, and gradually rebounds over 72 h (Figure 5B). At the endoplasmic reticulum (ER), Golgi, and mitochondria, basal Ras signaling is relatively low and increases over 72 h. To probe how sotorasib modulates the contribution of individual Ras isoforms to these

(C) Ras-less MEFs were transfected with their respective RIB for 1 day. These cells were compared to WT MEFs. These cells then underwent immunoblotting analysis. Right: densitometry quantification of immunoblots ($n = 3$ experiments). Analysis is normalized to vinculin loading control (i.e., pErk signal/vinculin signal or pan-Ras signal/vinculin signal). Statistics: two-way ordinary ANOVA. p values (from left to right): 0.038, 0.041, 0.03, and 0.027.
(D) MOLM-13 cell lines expressing either NRAS G12C or G12D were treated with or without doxycycline to induce mutant NRAS expression. Cells were also transfected with an NRAS RIB-expressing plasmid or empty vector and co-treated with AC220 (quizartinib, FLT3 inhibitor)[25,26] (see STAR Methods for details). Cells were then counted over a 7-day period ($n = 3$ experiments). Statistics: one-way ordinary ANOVA. p values (from left to right): 0.0057, 3.41×10^{-5}, and 5.2×10^{-7}.

Please cite this article in press as: Zhang et al., *De novo* design of Ras isoform selective binders, Cell Chemical Biology (2026), https://doi.org/10.1016/j.chembiol.2026.02.008

CellPress
OPEN ACCESS

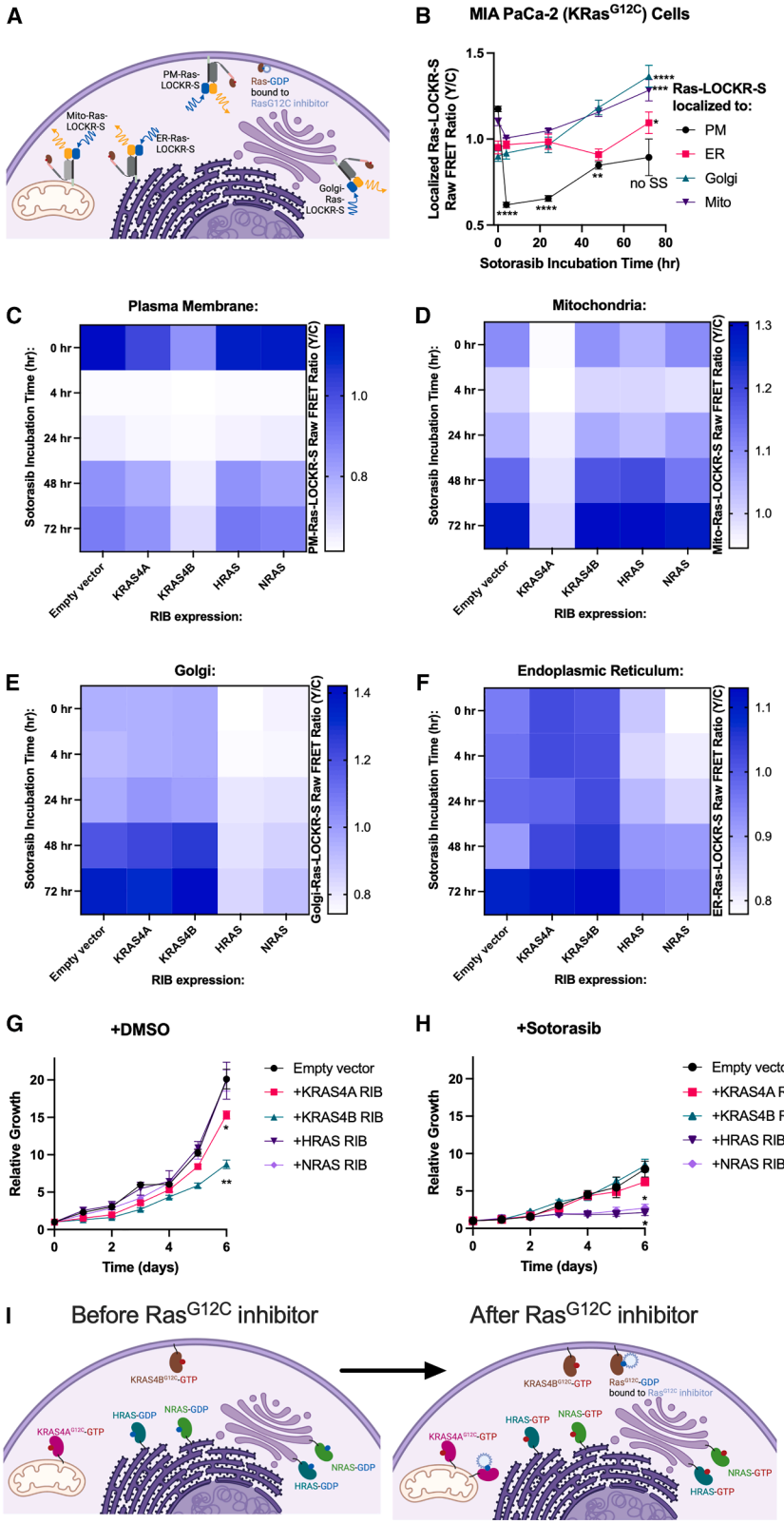

Figure 5. KRAS^{G12C}-mutant cancer cells switch dependency from mutant to wild-type Ras activity treatment with sotorasib

(A) Schematic of experimental setup. The genetically encodable Ras activity biosensor Ras-LOCKR-S can be subcellularly targeted to different subcellular regions by adding N-terminal localization sequences on the Ras-LOCKR-S Key protein. Subsequently, the Ras^{G12C} inhibitor sotorasib is added to the cells.

(B) MIA PaCa-2 cells (homozygous KRAS^{G12C}) were transfected with Ras-LOCKR-S targeted to the plasma membrane (PM), endoplasmic reticulum (ER), Golgi, or mitochondria (Mito). 1 day after transfection, cells were incubated with 100 nM sotorasib for up to 72 h and then subsequently imaged where the FRET ratio was calculated (n = 100 cells per condition). The middle line represents averages, and error bars represent SEM. Statistics: two-way ordinary ANOVA. p values (from left to right, top to bottom): 5.8×10^{-7}, 8.2×10^{-5}, 0.0045, 7.5×10^{-5}, 5.61×10^{-4}, and 0.017.

(C–F) MIA PaCa-2 cells expressing subcellularly localized Ras-LOCKR-S were co-transfected with empty vector or one of the RIBs. Ras-LOCKR-S was localized to the PM (C), mitochondria (D), Golgi (E), or ER (F). 1 day after transfection, cells were incubated with 100 nM sotorasib for up to 72 h and then subsequently imaged where the FRET ratio was calculated (n = 20 cells per condition). In the heatmap, dark blue represents relatively high average Ras-LOCKR-S FRET ratios while white represents relatively low average Ras-LOCKR-S FRET ratios.

(G and H) MIA PaCa-2 cells were transfected with either empty vector or one of the RIBs, underwent puromycin selection for 1 day, and then were treated with half-dose puromycin selection for the rest of the experiment. 2 days after puromycin selection, cells were either incubated with DMSO (G) or 100 nM sotorasib (H) and cells were counted every day (n = 3 experiments). The middle line represents averages, and error bars represent SEM. Statistics: two-way ordinary ANOVA. p values (from top to bottom, G to H): 0.032, 0.0057, 0.023, and 0.015.

(I) Summary of our results and working model. Prior to Ras^{G12C} inhibition, KRAS^{G12C}-mutated cells are dependent on mutant KRAS-driven signaling and cell growth. After Ras^{G12C} inhibition, these KRAS^{G12C}-mutated cells switch to be dependent on wild-type HRAS and NRAS-driven signaling and cell growth, thus still being addicted to Ras signaling.

Please cite this article in press as: Zhang et al., *De novo* design of Ras isoform selective binders, Cell Chemical Biology (2026), https://doi.org/10.1016/j.chembiol.2026.02.008

subcellular Ras activity dynamics, we performed the same experiment as in Figure 5B but with RIBs transfected. Strikingly, each subcellular region was most affected by a different Ras isoform. KRAS4B inhibition via KRAS4B RIB expression led to the largest decrease in basal Ras signaling at the PM and diminished PM-localized rebound Ras signaling after sotorasib treatment (Figure 5C). At the mitochondria, KRAS4A RIB expression led to decreased basal Ras signaling and prevented Ras activation after sotorasib treatment (Figure 5D). At the Golgi and ER, HRAS RIB or NRAS RIB expression both led to decreased basal Ras signaling and abrogated sotorasib-induced Ras activation (Figures 5E and 5F). These results indicate that each of these Ras isoforms primarily affect different subcellular pools of Ras during Ras^{G12C} inhibition: $KRAS4B^{G12C}$ is the dominant isoform that affects PM-localized Ras activities, $KRAS4A^{G12C}$ is most critical for mitochondria-localized Ras signaling, and WT HRAS and NRAS play a role in Golgi and ER-localized Ras signaling. Beyond Ras^{G12C} inhibition, this subcellular pattern of Ras isoform activities holds true also during EGF stimulation (Figures S9A–S9C).

To further probe into whether different Ras isoforms have distinct functional roles during Ras^{G12C} inhibition, RIBs were expressed in MIA PaCa-2 cells, and cell proliferation was recorded either without or with sotorasib (Figures 5G and 5H). In the absence of sotorasib, the MIA PaCa-2 cells grow exponentially, with a 20.1-fold increase in number of cells present 6 days after initial seeding. In these conditions, KRAS4B inhibition through KRAS4B RIB expression led to the most significant decrease in cell proliferation (to 8.7 times fewer cells 6 days after initial seeding). KRAS4A RIB expression led to a statistically significant decrease in cell proliferation, to 15.3 times fewer cells 6 days after initial seeding in $KRAS^{G12C}$-mutant MIA PaCa-2 cells. As expected, HRAS and NRAS RIB expression led to no significant change in cell proliferation. These data suggest that prior to Ras^{G12C} inhibition, the cell proliferation of $KRAS^{G12C}$-mutant cells is most dependent on KRAS4B signaling. However, this Ras isoform dependency switches during Ras^{G12C} inhibition. With sotorasib present, cells proliferate at a slower rate with 8.4 times fewer cells recovered 6 days after initial seeding. During continuous sotorasib exposure, neither KRAS4B nor KRAS4A RIB expression led to significant changes in cell proliferation. By contrast, both HRAS or NRAS RIB expression led to significant decreases in cell proliferation to 2.1 and 2.8 times fewer cells recovered 6 days after initial seeding, respectively. These cell growth results were recapitulated in another $KRAS^{G12C}$-mutant cell line SW1573 (Figures S9D and S9E).

These data support the working model shown in Figure 5I in which hyperactive KRAS4B signaling at the PM and KRAS4A signaling at the mitochondria drive the aberrant growth of $KRAS^{G12C}$-mutant cancer cells. Upon Ras^{G12C} inhibition, $KRAS^{G12C}$-mutant cells partially reactivate KRAS4B at the PM and KRAS4A at the mitochondria. Strikingly, Sotorasib treatment also markedly reduced the growth of cells expressing HRAS or NRAS RIBs. These data suggest that $KRAS^{G12C}$-mutant cancer cells adapt to RasG12C inhibition by activating WT HRAS and NRAS signaling at the Golgi and ER. We speculate that WT HRAS and NRAS signaling might contribute to the development of drug resistance by allowing cancer cells to survive and proliferate at low levels until they acquire resistance mutations in *BRAF*, *NRAS*, and other genes that restore oncogenic MAPK signaling. Accordingly, co-targeting mutant KRAS and WT NRAS and/or HRAS may circumvent RasG12C inhibitor resistance.

DISCUSSION

Tools that can differentiate Ras isoforms in normal and diseased cells have been lacking due to the high sequence similarity between the isoforms except at their C terminus. Commercially available antibodies that claim to be isoform selective often show nonspecificity (Figure S4). Several engineered proteins targeting Ras do exist such as Designed Ankyrin Repeat Proteins,[34] Affimers,[35] and Monobodies[6,36,37] that either stabilize or inhibit Ras, but these target the structured portion of Ras and not its disordered C terminus and thus are not isoform selective. To address this important challenge, we *de novo* designed RIBs that bind to these highly charged and disordered C termini with higher specificity than any reagents described to date[5,6] both *in vitro* and in cells. Targeting highly polar regions is difficult due to competing with water solvation, and these C-terminal targets are among the most polar targets that protein binder design has addressed (for example, the KRAS4B C terminus is ~80% polar residues). Expression of the RIBs selectively enhanced the cytosolic localization of individual Ras isoforms, which led to decreased Ras activity consistent with the requirement for membrane association for Ras function. Using the RIBs as Ras isoform-selective inhibitors, we discovered that each isoform is activated at a distinct subcellular region, which has functional consequences during Ras^{G12C} inhibition. Our results suggest that during RasG12C inhibition, $KRAS^{G12C}$-mutant cancers become dependent on WT HRAS and NRAS signaling for proliferation. This is notable because these cells express all four major Ras isoforms, allowing for potential compensatory signaling when one isoform is inhibited. Despite this, we still observe a marked reduction in Ras signaling upon inhibition of a single isoform, indicating that certain Ras isoforms exert dominant effects and underscoring the utility of RIBs. At the same time, compensatory activity from other isoforms may limit the therapeutic potential of RIBs. One approach to enhance their potency could be to link them with ubiquitin ligase-recruiting modules to function as bioPROTACs. Alternatively, pan-Ras inhibitors have been developed and may provide a more effective strategy for targeting Ras-addicted cancers, though at the cost of reduced specificity and a narrower therapeutic window. The ability of cancer cells to persist and expand during treatment further promotes the emergence of resistance mutations and tumor regrowth. Together, these results suggest that targeting normal GTP-loaded HRAS and NRAS with pan-Ras inhibitors like daraxonrasib[38] may represent a viable strategy to enhance the efficacy of sotorasib and other selective RasG12C inhibitors.

In addition to providing valuable tools for understanding Ras subcellular localization and how it is altered by treatment with sotorasib and other drugs, the RIBs could serve as a starting point for developing isoform-specific therapeutics. For example, some of our binders have preference for the non-palmitoylated version of Ras C terminus (e.g., KRAS4A and NRAS binders, Figures S3I and S6). The palmitoylation/depalmitoylation cycle is a promising therapeutic target in *NRAS*-mutant cancers,[31–33] and our NRAS RIBs may inform structure/function studies to develop selective C181S binders. RIB-based scaffolds may

also address the difficult challenge of co-targeting KRAS4A and KRAS4B in *KRAS*-mutant cancers.

In summary, given the central importance of hyperactive Ras in signal transduction, RASopathy developmental disorders, and cancer, our Ras isoform-selective binders should be useful for a wide range of applications including the development of isoform specific inhibitors, providing affinity handles for targeted degradation, informing new diagnostic markers for cancer samples, and as Ras isoform-specific activity sensors. More broadly, this study further validates *de novo* protein design as a robust strategy for targeting disordered clinically relevant therapeutic targets, and for generating chemical biology tools to disentangle the biological roles of closely related proteins.

Limitations of the study

There are two limitations of the design methodology that we anticipate will soon be overcome. First, the percentage of tested designs that bound to target is low (KRAS4A: 3%, KRAS4B: 0.78%, HRAS: 4%, and NRAS: 2.9%)—with improved models and feedback from these and other binder design experiments, it should be possible to improve the methods and increase success rates. Second, the design calculations were done against the unmodified C termini where farnesylation and palmitoylation were not included and the membrane context was not considered; hence, these binders likely only recognize a subset of RAS molecules (Figures S3I and S6) and potentially bias the localization changes of RAS when expressed in cells (Figure 4A). However, all the binders are capable of binding to the farnesylated Ras C terminus, and the HRAS RIB can bind to palmitoylated HRAS (Figures S3E and S3I) (note that KRAS4B does not get palmitoylated). With the recent development of all-atom RFDiffusion,[39] it should soon become possible to design binders against the covalently modified versions, enabling separate tracking of the pools of lipidated and non-lipidated molecules for each isoform. In terms of the technical aspects of our article, we do not provide structural data; thus, it is unclear how accurate our design models are. The Ras^{G12C} inhibition studies were done in homozygous $KRAS^{G12C}$-mutated cells, and the importance of other Ras isoforms during Ras^{G12C} inhibition in heterozygous $KRAS^{G12C}$-mutated cells is unclear. Finally, for potential therapeutic applications, direct delivery of proteins into the cytoplasm is still very challenging, but recent advances in viral and mRNA delivery now provide a route to targeted expression of the RIBs in the cytoplasm for specific RAS isoform inhibition.

RESOURCE AVAILABILITY

Lead contact

Further information and requests for resources and reagents should be directed to and will be fulfilled by the lead contact, Jason Z. Zhang (jzz0428@g.ucla.edu).

Materials availability

All plasmids generated in this study are available from the lead contact with a completed materials transfer agreement.

Data and code availability

- The data and design models that support the findings of this study will be available from Zenodo: https://doi.org/10.5281/zenodo.18322184. Sequencing data in Table S1 will be uploaded in Zenodo.
- This article does not report original code.
- Any additional information required to reanalyze the data reported in this paper is available from the lead contact upon request.

ACKNOWLEDGMENTS

We acknowledge funding from HHMI (J.Z.Z. and D.B.), Helen Hay Whitney Foundation (J.Z.Z.), NCI R00-CA293001 (J.Z.Z.), the Croucher Fellowship (H.J.), the Audacious Project at the Institute for Protein Design (J.Z.Z. and D.B.), NIH K08-CA256489 (B.J.H.), and NIH R01 CA193994 (K.S. and B.J.H.). We thank D.J. Maly, F. McCormick, and D. Esposito for fruitful discussion of the Ras results, C.M. Dobbins and S. Cheng for help with mammalian cells and cell culture, and the RAS Initiative at the Frederick National Lab for providing the MEF cells.

AUTHOR CONTRIBUTIONS

J.Z.Z. conceived of the project. K.W. supervised design strategies for making RIBs in this work, designed and assembled templates for KRAS4B, and designed the scaffolds used in the logos pipeline. J.Z.Z. computationally designed these proteins with help from K.W., H.J., and C.L. J.Z.Z. and D.B. supervised, designed, and interpreted the experiments. J.Z.Z. performed all the experiments. X.L. made the Ras isoform peptides. J.Z.Z. and D.B. wrote the original draft. All authors reviewed and commented on the manuscript.

DECLARATION OF INTERESTS

The authors declare no competing interests.

STAR★METHODS

Detailed methods are provided in the online version of this paper and include the following:

- KEY RESOURCES TABLE
- EXPERIMENTAL MODEL AND STUDY PARTICIPANT DETAILS
  - Cell lines
- METHOD DETAILS
  - Amino acid recognition pocket based design and scaffolded RFDiffusion
  - Sequence input RFDiffusion based design
  - Peptide generation
  - DNA library preparation
  - Yeast surface display
  - Cell transfection and siRNA information
  - General procedures for bacterial protein production and purification
  - Biolayer interferometry
  - Immunostaining
  - Membrane fractionation
  - Immunoblotting and immunoprecipitation
  - Epifluorescence imaging
  - Co-localization analysis
  - MOLM-13 cell line generation and cell growth assays
  - Graphics
- QUANTIFICATION AND STATISTICAL ANALYSIS
  - Statistics and reproducibility

SUPPLEMENTAL INFORMATION

Supplemental information can be found online at https://doi.org/10.1016/j.chembiol.2026.02.008.

Received: July 8, 2025
Revised: November 22, 2025
Accepted: February 17, 2026

REFERENCES

1. Nissley, D.V., and McCormick, F. (2022). RAS at 40: update from the RAS initiative. Cancer Discov. *12*, 895–898.
2. Zhang, J.Z., Ong, S.-E., Baker, D., and Maly, D.J. (2025). Single-cell sensor analyses reveal signaling programs enabling Ras-G12C drug resistance. Nat. Chem. Biol. *21*, 47–58.
3. Choy, E., Chiu, V.K., Silletti, J., Feoktistov, M., Morimoto, T., Michaelson, D., Ivanov, I.E., and Philips, M.R. (1999). Endomembrane trafficking of ras: the CAAX motif targets proteins to the ER and Golgi. Cell *98*, 69–80.
4. Amendola, C.R., Mahaffey, J.P., Parker, S.J., Ahearn, I.M., Chen, W.C., Zhou, M., Court, H., Shi, J., Mendoza, S.L., Morten, M.J., et al. (2019). KRAS4A directly regulates hexokinase 1. Nature *576*, 482–486.
5. Waters, A.M., Ozkan-Dagliyan, I., Vaseva, A.V., Fer, N., Strathern, L.A., Hobbs, G.A., Tessier-Cloutier, B., Gillette, W.K., Bagni, R., Whiteley, G.R., et al. (2017). Evaluation of the selectivity and sensitivity of isoform- and mutation-specific RAS antibodies. Sci. Signal. *10*, eaao3332.
6. Whaby, M., Ketavarapu, G., Koide, A., Mazzei, M., Mintoo, M., Glasser, E., Patel, U., Nasarre, C., Sale, M.J., McCormick, F., et al. (2024). Inhibition and degradation of NRAS with a pan-NRAS monobody. Oncogene *43*, 3489–3497.
7. Watson, J.L., Juergens, D., Bennett, N.R., Trippe, B.L., Yim, J., Eisenach, H.E., Ahern, W., Borst, A.J., Ragotte, R.J., Milles, L.F., et al. (2023). De novo design of protein structure and function with RFdiffusion. Nature *620*, 1089–1100.
8. Dauparas, J., Anishchenko, I., Bennett, N., Bai, H., Ragotte, R.J., Milles, L.F., Wicky, B.I.M., Courbet, A., de Haas, R.J., Bethel, N., et al. (2022). Robust deep learning–based protein sequence design using ProteinMPNN. Science *378*, 49–56.
9. Baek, M., DiMaio, F., Anishchenko, I., Dauparas, J., Ovchinnikov, S., Lee, G.R., Wang, J., Cong, Q., Kinch, L.N., Schaeffer, R.D., et al. (2021). Accurate prediction of protein structures and interactions using a three-track neural network. Science *373*, 871–876.
10. Wu, K., Bai, H., Chang, Y.T., Redler, R., McNally, K.E., Sheffler, W., Brunette, T.J., Hicks, D.R., Morgan, T.E., Stevens, T.J., et al. (2023). De novo design of modular peptide-binding proteins by superhelical matching. Nature *616*, 581–589.
11. Wu, K., Jiang, H., Hicks, D.R., Liu, C., Muratspahić, E., Ramelot, T.A., Liu, Y., McNally, K., Kenny, S., Mihut, A., et al. (2025). Design of intrinsically disordered region binding proteins. Science *389*, eadr8063.
12. Liu, C., Wu, K., Choi, H., Han, H.L., Zhang, X., Watson, J.L., Ahn, G., Zhang, J.Z., Shijo, S., Good, L.L., et al. (2025). Diffusing protein binders to intrinsically disordered proteins. Nature *644*, 809–817.
13. Vázquez Torres, S., Leung, P.J.Y., Venkatesh, P., Lutz, I.D., Hink, F., Huynh, H.H., Becker, J., Yeh, A.H.W., Juergens, D., Bennett, N.R., et al. (2024). De novo design of high-affinity binders of bioactive helical peptides. Nature *626*, 435–442.
14. Jiang, H., Jude, K.M., Wu, K., Fallas, J., Ueda, G., Brunette, T.J., Hicks, D.R., Pyles, H., Yang, A., Carter, L., et al. (2024). De novo design of buttressed loops for sculpting protein functions. Nat. Chem. Biol. *20*, 974–980.
15. Jumper, J., Evans, R., Pritzel, A., Green, T., Figurnov, M., Ronneberger, O., Tunyasuvunakool, K., Bates, R., Žídek, A., Potapenko, A., et al. (2021). Highly accurate protein structure prediction with AlphaFold. Nature *596*, 583–589.
16. Cao, L., Goreshnik, I., Coventry, B., Case, J.B., Miller, L., Kozodoy, L., Chen, R.E., Carter, L., Walls, A.C., Park, Y.J., et al. (2020). De novo design of picomolar SARS-CoV-2 miniprotein inhibitors. Science *370*, 426.
17. Cao, L., Coventry, B., Goreshnik, I., Huang, B., Sheffler, W., Park, J.S., Jude, K.M., Marković, I., Kadam, R.U., Verschueren, K.H.G., et al. (2022). Design of protein-binding proteins from the target structure alone. Nature *605*, 551–560.
18. Lanning, C.C., Daddona, J.L., Ruiz-Velasco, R., Shafer, S.H., and Williams, C.L. (2004). The Rac1 C-terminal polybasic region regulates the nuclear localization and protein degradation of Rac1. J. Biol. Chem. *279*, 44197–44210.
19. Barceló, C., Paco, N., Morell, M., Alvarez-Moya, B., Bota-Rabassedas, N., Jaumot, M., Vilardell, F., Capella, G., and Agell, N. (2014). Phosphorylation at Ser-181 of oncogenic KRAS is required for tumor growth. Cancer Res. *74*, 1190–1199.
20. Drosten, M., Dhawahir, A., Sum, E.Y.M., Urosevic, J., Lechuga, C.G., Esteban, L.M., Castellano, E., Guerra, C., Santos, E., and Barbacid, M. (2010). Genetic analysis of Ras signalling pathways in cell proliferation, migration and survival. EMBO J. *29*, 1091–1104.
21. Burgan, W., and Fer, N. (2024). Creation of an Isogenic H/N/KRAS-Less Mouse Embryonic Fibroblast Cell Line Panel Derived from a Size-Sorted Diploid Clone. In KRAS: Methods and Protocols, pp. 323–336.
22. Prior, I.A., and Hancock, J.F. (2012). Ras trafficking, localization and compartmentalized signalling. Semin. Cell Dev. Biol. *23*, 145–153.
23. Zambetti, N.A. (2017). Genetic Validation of the Palmitoylation/Depalmitoylation Cycle As a Drug Target in NRAS Mutant Hematologic Malignancies In Vivo. Blood *130*, 1221.
24. Tulpule, A., Guan, J., Neel, D.S., Allegakoen, H.R., Lin, Y.P., Brown, D., Chou, Y.T., Heslin, A., Chatterjee, N., Perati, S., et al. (2021). Kinase-mediated RAS signaling via membraneless cytoplasmic protein granules. Cell *184*, 2649–2664.e18.
25. Harris, M., Huang, B.J., Harris, M., Boone, C., Wang, W., Carias, H., Mesiona, B., Mavrici, D., Kohler, A.C., Bollag, G., et al. (2023). Structural and functional analyses of a germline KRAS T50I mutation provide insights into Raf activation. JCI Insight *8*, e168445.
26. Morstein, J., Bowcut, V., Fernando, M., Yang, Y., Zhu, L., Jenkins, M.L., Evans, J.T., Guiley, K.Z., Peacock, D.M., Krahnke, S., et al. (2024). Targeting Ras-Rho-and Rab-family GTPases via a conserved cryptic pocket. Cell *187*, 6379–6392.e17.
27. Lynch, S.J., Snitkin, H., Gumper, I., Philips, M.R., Sabatini, D., and Pellicer, A. (2015). The differential palmitoylation states of N-Ras and H-Ras determine their distinct Golgi subcompartment localizations. J. Cell. Physiol. *230*, 610–619.
28. Augsten, M., Pusch, R., Biskup, C., Rennert, K., Wittig, U., Beyer, K., Blume, A., Wetzker, R., Friedrich, K., and Rubio, I. (2006). Live-cell imaging of endogenous Ras-GTP illustrates predominant Ras activation at the plasma membrane. EMBO Rep. *7*, 46–51.
29. Zhang, J.Z., Nguyen, W.H., Greenwood, N., Rose, J.C., Ong, S.E., Maly, D.J., and Baker, D. (2024). Computationally designed sensors detect endogenous Ras activity and signaling effectors at subcellular resolution. Nat. Biotechnol. *42*, 1888–1898.
30. Chiu, V.K., Bivona, T., Hach, A., Sajous, J.B., Silletti, J., Wiener, H., Johnson, R.L., 2nd, Cox, A.D., and Philips, M.R. (2002). Ras signalling on the endoplasmic reticulum and the Golgi. Nat. Cell Biol. *4*, 343–350.
31. Rowinsky, E.K., Windle, J.J., and Von Hoff, D.D. (1999). Ras protein farnesyltransferase: a strategic target for anticancer therapeutic development. J. Clin. Oncol. *17*, 3631–3652.
32. Remsberg, J.R., Suciu, R.M., Zambetti, N.A., Hanigan, T.W., Firestone, A.J., Inguva, A., Long, A., Ngo, N., Lum, K.M., Henry, C.L., et al. (2021). ABHD17 regulation of plasma membrane palmitoylation and N-Ras-dependent cancer growth. Nat. Chem. Biol. *17*, 856–864.
33. Zambetti, N.A., Firestone, A.J., Remsberg, J.R., Huang, B.J., Wong, J.C., Long, A.M., Predovic, M., Suciu, R.M., Inguva, A., Kogan, S.C., et al. (2020). Genetic disruption of N-RasG12D palmitoylation perturbs hematopoiesis and prevents myeloid transformation in mice. Blood *135*, 1772–1782.
34. Guillard, S., Kolasinska-Zwierz, P., Debreczeni, J., Breed, J., Zhang, J., Bery, N., Marwood, R., Tart, J., Overman, R., Stocki, P., et al. (2017). Structural and functional characterization of a DARPin which inhibits Ras nucleotide exchange. Nat. Commun. *8*, 16111.
35. Haza, K.Z., Martin, H.L., Rao, A., Turner, A.L., Saunders, S.E., Petersen, B., Tiede, C., Tipping, K., Tang, A.A., Ajayi, M., et al. (2021). RAS-inhibiting

biologics identify and probe druggable pockets including an SII-α3 allosteric site. Nat. Commun. *12*, 4045.

36. Teng, K.W., Tsai, S.T., Hattori, T., Fedele, C., Koide, A., Yang, C., Hou, X., Zhang, Y., Neel, B.G., O'Bryan, J.P., and Koide, S. (2021). Selective and noncovalent targeting of RAS mutants for inhibition and degradation. Nat. Commun. *12*, 2656.
37. Alshahrani, M., Parikh, V., Foley, B., Hu, G., and Verkhivker, G. (2025). Atomistic Profiling of KRAS Interactions with Monobodies and Affimer Proteins Through Ensemble-Based Mutational Scanning Unveils Conserved Residue Networks Linking Cryptic Pockets and Regulating Mechanisms of Binding, Specificity and Allostery. Preprint at bioRxiv. https://doi.org/10.1101/2025.03.11.642708.
38. Holderfield, M., Lee, B.J., Jiang, J., Tomlinson, A., Seamon, K.J., Mira, A., Patrucco, E., Goodhart, G., Dilly, J., Gindin, Y., et al. (2024). Concurrent inhibition of oncogenic and wild-type RAS-GTP for cancer therapy. Nature *629*, 919–926.
39. Krishna, R., Wang, J., Ahern, W., Sturmfels, P., Venkatesh, P., Kalvet, I., Lee, G.R., Morey-Burrows, F.S., Anishchenko, I., Humphreys, I.R., et al. (2024). Generalized biomolecular modeling and design with RoseTTAFold All-Atom. Science *384*, eadl2528.

Please cite this article in press as: Zhang et al., *De novo* design of Ras isoform selective binders, Cell Chemical Biology (2026), https://doi.org/10.1016/j.chembiol.2026.02.008

STAR★METHODS

KEY RESOURCES TABLE

REAGENT or RESOURCE	SOURCE	IDENTIFIER
Antibodies		
Ms anti-Erk	Cell Signaling Technology (CST)	Cat#9107
Rb anti-phospho-Erk	CST	Cat#9101
Ms anti-Akt	CST	Cat#2920
Rb anti-phospho-Akt (S473)	CST	Cat#9271
Rb anti-GAPDH	CST	Cat#5174
Ms anti-Vinculin	Sigma-Aldrich	Cat#V9131
Ms anti-Myc Tag	CST	Cat#2276
Ms anti-Flag Tag	Sigma-Aldrich	Cat#A8592
Rb anti-E cadherin	Abcam	Cat#ab40772
Ms anti-Giantin	Abcam	Cat#ab37266
Rb anti-pan Ras	CST	Cat#91054
Rb anti-GFP	CST	Cat#2555
Rb anti-Hsp90	CST	Cat#4877
Rb anti-Caveolin-1	CST	Cat#3267
Streptavidin, Alexa Fluor™ 488 conjugate	ThermoFisher	Cat#S11223
anti-C-Myc Antibody (Chicken) - FITC Conjugated	ICL	Cat#CMYC-45F
680 RD anti-Ms	LICOR	Cat#26-68071
680 RD anti-Rb	LICOR	Cat#926-68070
800 CW anti-Ms	LICOR	Cat#926-32210
800 CW anti-Rb	LICOR	Cat#926-32211
AF488 anti-Ms	Thermo Fisher	Cat#A11029
AF568 anti-Rb	Thermo Fisher	Cat#A11036
AF488 anti-Rb	Thermo Fisher	Cat#A11034
AF750 anti-Ms	Thermo Fisher	Cat#A21037
Streptavidin, R-Phycoerythrin Conjugate (SAPE)	Life Technologies	Cat#S866
Rb anti-KRAS4A	Millipore Sigma	Cat#ABC1442
Ms anti-KRAS4B	Sigma-Aldrich	Cat#WH0003845M1
Rb anti-HRAS	ProteinTech	Cat#18295-1-AP
Ms anti-NRAS	SCBT	Cat#SC-31
Bacterial and virus strains		
E. coli Lemo21(DE3)	NEB	Cat#C2528J
Chemicals, peptides, and recombinant proteins		
Fugene HD Transfection Reagent	Fugene	Cat#E2311
Poly-D-Lysine	MP Biomedical	Cat#215017580
RIPA Buffer	Thermo Fisher	Cat#89901
Pierce™ High Capacity Streptavidin Agarose	Thermo Fisher	Cat#20359
Lipofectamine™ LTX Reagent with PLUS™ Reagent	Thermo Fisher	Cat#15338100
Turbofectin 8.0	Origene	Cat#TF81001
Electroporation Buffer	MaxCyte	Cat#EPB-5
16% PFA	Electron Microscopy Services	Cat#15710
Trans-Blot Turbo Transfer Pack	BioRad	Cat#1704159
Pierce Protease Inhibitor Tablets	Thermo Fisher	Cat#A32963
PHEM 0.2M	Electron Microscopy Services	Cat#11165

(*Continued on next page*)

Please cite this article in press as: Zhang et al., *De novo* design of Ras isoform selective binders, Cell Chemical Biology (2026), https://doi.org/10.1016/j.chembiol.2026.02.008

Continued

REAGENT or RESOURCE	SOURCE	IDENTIFIER
Biotin	Sigma-Aldrich	Cat#B4501
0.25% Trypsin-EDTA	Gibco	Cat#25200072
Pageruler Prestained Ladder	Thermo Fisher	Cat#PI26620
Spectra™ Multicolor High Range Protein Ladder	Thermo Fisher	Cat#26625
Protein A Agarose Beads	CST	Cat#9863S
Protein G Agarose Beads	CST	Cat#37478
Puromycin	Tocris	Cat#4089
Hygromycin	Tocris	Cat#4137
DPBS	Gibco	Cat#14190250
Doxycycline	Tocris	Cat#4090
Studier Induction Media	Teknova	Cat#3S8000
Kanamycin	Millipore Sigma	Cat#PHR1487
Ni-NTA resin	Qiagen	Cat#30250
Ultra-15 Centrifugal Filter Units	Amicon	Cat#UFC9100
Superdex 75 Increase 10/300 GL	GE Healthcare	Cat#29148721
EGF	Thermo Fisher	Cat#PHG0311
Polydiallyldimethylammonium	Sigma-Aldrich	Cat#409014
Talon cobalt affinity resin	Takara Bio	Cat#635653
Cytiva S200 Increase column	Sigma-Aldrich	Cat#GE28-9909-44
DAPI	ThermoFisher	Cat#62248
FluoroBrite DMEM Media	GIBCO	Cat#A1896701
FBS	Sigma-Aldrich	Cat#F2442
Pen-Strep	Sigma-Aldrich	Cat#P4333
RPMI 1640	GIBCO	Cat#11875093
PEI Max	PolyScience	Cat#24765
Cell Fractionation Kit	CST	Cat#9038
FGTI-2734	MedChemExpress	Cat#HY-128350
AC220	MedChemExpress	Cat#HY-13001
AMG-510	Selleck Chem	Cat#S8830
Deposited data		
Zenodo	This Paper	https://doi.org/10.5281/zenodo.18322184
Experimental models: Cell lines		
HEK293T	ATCC	Cat#CRL-3216
HeLa	ATCC	Cat#CCL-2
H2228	Gift from R. Bayliss lab	N/A
KRas4A WT MEF	NCI	Cat#RPZ26187
KRas4B WT MEF	NCI	Cat#RPZ25854
HRas WT MEF	NCI	Cat#RP200024
NRas WT MEF	NCI	Cat#RPZ26379
MIA PaCa-2	ATCC	Cat#CRL-1420
H358	ATCC	Cat#CRL-5807
MOLM-13 Cells	DSMZ	Cat#ACC-554
H441	ATCC	Cat#HTB-174
Rh36	Gift from DJ. Maly lab	N/A
RD	ATCC	Cat#CCL-136
H1299	Gift from R. Bayliss lab.	N/A
SW1573	ATCC	Cat#CRL-2170
Experimental models: Organisms/strains		
S. cerevisiae EBY100	ATCC	Cat#MYA-4941DQ

(*Continued on next page*)

Continued

REAGENT or RESOURCE	SOURCE	IDENTIFIER
Software and algorithms		
Pymol	Schrodinger Inc	Version 2.6
Biorender	BioRender	www.biorender.com

EXPERIMENTAL MODEL AND STUDY PARTICIPANT DETAILS

Cell lines

HEK293T (Female), HeLa (Female), MEF (Mixed, pool of mouse embryos), Rasless MEF (Mixed, pool of mouse embryos) (isogenic cell lines, derived from Cell line DU1473 mouse embryonic fibroblast (MEF); $Hras^{-/-}$; $Nras^{-/-}$; $Kras^{lox/lox}$; $RERT^{ert/ert}$),[21] MIA PaCa-2 (Male), H358 (Male), H441 (Female), Rh36 (Male), RD (Male), H1299 (Male) cell lines were cultured in Dulbecco's modified Eagle medium (DMEM) containing 1 g L^{-1} glucose and supplemented with 10% (v/v) fetal bovine serum (FBS) and 1% (v/v) penicillin–streptomycin (Pen-Strep). H2228 (Female), SW1573 (Female), and MOLM-13 cells (Male) were grown in RPMI-1640 cell media containing 1 g L^{-1} glucose and supplemented with 10% (v/v) fetal bovine serum (FBS) and 1% (v/v) penicillin–streptomycin (Pen-Strep). For MOLM-13 cells, 2mM glutamine was also added to the media. All cells were grown in a humidified incubator at 5% CO_2 and at 37°C. All cell lines were obtained directly from ATCC, were not further authenticated after purchase, and were routinely inspected for mycoplasma contamination.

METHOD DETAILS

Amino acid recognition pocket based design and scaffolded RFDiffusion

Amino acid recognition pocket based design: Logos library A

As described in the previous work featuring the logos pipeline,[10,11] the recognition pocket approach took advantage of the overall flexible nature of disordered regions as well as the base of amino acid recognition in a string of polymers. In short, this approach would thread the query target into a diverse and robust family of ~1,000 *de novo* protein-peptide complex templates, made up of arbitrary combos of 20 amino acid recognition pockets assembled into computationally designed universal binding modes. Initial docks were judged by how well fit each individual amino acid from the query target was, and how many of those fits were out of non-fits. Top docks were then identified by the pipeline, which were considered as the best design starting points. Sequence design, structural prediction, RFdiffusion refinement were then applied sequentially, until new customizable binding proteins were made and predicted well to the query target of interest.

Scaffolded RFDiffusion: Logo library B

A subset of ~200 β-sheet containing templates derived from the amino acid recognition pocket based design of template backbones (logos library B) were used as the starting point. These templates then went through the same pipeline as described above of peptide threading, sequence design, predictions, and then diffusion refinement.

Sequence design

All accepted docks are sent to ProteinMPNN with a customized script that applies empirical weights to certain amino acids. Two iterations of ProteinMPNN and FastRelax are performed to adjust designed protein backbones further and optimize the binder SAP score (SAP < 35). Sequences with the lowest ProteinMPNN scores are filtered and sent to our customized AF2 package. This filtering process varies depending on the target's difficulty level. Criteria can be adjusted based on individual targets and design campaigns. Subsequently, FastRelax was employed to obtain Rosetta metrics. The resulting binders were further filtered according to specific criteria, including contact molecular surface (CMS) (CMS > 180Å^2 for KRAS4A, CMS > 200Å^2 for NRAS, CMS > 140Å^2 for KRAS4B and HRAS), ddG (ddG < -80 for KRAS4A and NRAS, ddG < -50 for KRAS4B and HRAS), SAP score (SAP < 35), and the number of hydrogen bonds (num_hbond) (num_hbond > 4). These filtering criteria were meticulously chosen to narrow the selection down.

Predictions

After two cycles of sequence design and AF2 (prediction-guided sequence design), passing designs undergo AlphaFold-multimer for final predictions. For highly polar or proline-rich targets, AlphaFold-multimer proved more predictive than AlphaFold-initial guess. These designs were then filtered based on interface pAE (pAE < 7 for KRAS4A and NRAS, pAE < 12 for KRAS4B and HRAS) and pLDDT (pLDDT < 87 for KRAS4A and NRAS, pLDDT < 80 for KRAS4B and HRAS). AlphaFold-monomer is then applied to assess designed monomer predictions and select the final designs for experimental testing. AF2 monomer filtering was based on the binder's monomer pLDDT (pLDDT < 90 for KRAS4A and NRAS, pLDDT < 82 for KRAS4B and HRAS) and RMSD (RMSD < 4.5Å) relative to the binder design model.

Sequence input RFDiffusion based design

Initial sequence input RFDiffusion and sequence design

For each target, approximately 10,000-50,000 diffused designs were generated based solely on the sequence input of the target. The resulting backbone library was subjected to sequence design using ProteinMPNN, followed by AF2 initial guess. These designs were

Please cite this article in press as: Zhang et al., *De novo* design of Ras isoform selective binders, Cell Chemical Biology (2026), https://doi.org/10.1016/j.chembiol.2026.02.008

then filtered based on interface pAE (pAE < 5 for KRAS4A and NRAS, pAE < 10 for KRAS4B and HRAS) and pLDDT (pLDDT < 90 for KRAS4A and NRAS, pLDDT < 80 for KRAS4B and HRAS). Additionally, AF2 monomer analysis was conducted using only the binder sequence without the peptide, allowing for filtering based on the binder's monomer pLDDT (pLDDT < 92 for KRAS4A and NRAS, pLDDT < 85 for KRAS4B and HRAS) and RMSD (RMSD < 5Å) relative to the binder design model. Subsequently, FastRelax was employed to obtain Rosetta metrics. The resulting binders were further filtered according to specific criteria, including contact molecular surface (CMS) (CMS > 200Å^2 for KRAS4A, CMS > 250Å^2 for NRAS, CMS > 150Å^2 for KRAS4B and HRAS), ddG (ddG < -70 for KRAS4A and NRAS, ddG < -50 for KRAS4B and HRAS), SAP score (SAP < 35), and the number of hydrogen bonds (num_hbond) (num_hbond > 5). These filtering criteria were meticulously chosen to narrow the selection down.

Backbone optimization with RFDiffusion and parametric perturbation

The process of pocket recognition and assembly played a crucial role in refining precise interactions with individual amino acids in a sequence-specific manner. This was particularly important when dealing with challenging polar or charged targets or targets that would not form regular secondary structures upon binding.

Motif RFDiffusion

As described in the previous work of *logos* pipeline,[10,11] if the design did not meet the complex prediction criteria mentioned above, or if a larger number of tested designs was preferred, motif RFDiffusion was employed to optimize the fit between less-than-ideal interacting pockets and binder backbones. In this work, especially for the need of yeast display screening thousands of binders a time, we used motif RFDiffusion more dramatically than originally developed to meanwhile shrink the binder size. Here, we retained a significant portion of the original binding interactions and motifs mostly around the central part of the RIBs to preserve the advantages of our general platform. Meanwhile, we deleted the terminal region and let RFDiffusion regrow with a smaller length. As part of this strategy, we developed partial RFDiffusion with small steps and multi-motif-constrained RFDiffusion (motif RFDiffusion).

Partial RFDiffusion (one-sided)

As in other cases, RFDiffusion was modified to allow the input structure to be noised only up to a user-specified time step, rather than completing the full noising schedule. Consequently, the denoising trajectory's starting point retained information about the input distribution, leading to denoised structures that remained structurally similar to the original input. In our work, the time step was set lower to maintain structural similarity, given that the high design resolution of hydrogen bonding interactions (especially with polar amino acids) was deemed critical. Specifically, 10-18 noising timesteps (10, 12, 15, 18) out of a total of 50 were selected for this paper's work. For each target parameter, 200 to 3,000 partially diffused designs were generated.

The new backbones were then subjected to ProteinMPNN sequence design and AF2 predictions, as previously described. These designs were filtered using the same criteria, with the observation that partial RFDiffusion tended to increase the overall number of passing designs. However, it was also noted that the original hydrogen bonding networks (particularly bidentate hydrogen bonds to the target backbone) were sometimes disrupted without being detected by AF2. To address this, we implemented an additional filter, 'buns' (buried unsatisfied hydrogen bonds) <=1, to explicitly count unsatisfied heavy atoms. Depending on the target's polarity, this step could filter out 50-80% of designs.

Parametric perturbation

Helices that were suboptimal in terms of interaction with the target could be isolated from the binder template and underwent defined x/y/z translations and rotations. Rosetta-based scoring of these translations and rotations filtered perturbations that were either non-productive (moved the helix too far away from the target) or clashed with the target. Then motif RFDiffusion was used to connect the perturbed helix to the rest of the binder template.

Peptide generation

All Fmoc-protected amino acids were obtained from P3 Biosystems; the coupling reagent HATU, DIPEA, and other chemicals unless otherwise stated were obtained from Sigma-Aldrich; DIC was obtained from Oakwood Chemicals; acetonitrile (ACN), methylene chloride (DCM), diethyl ether, and DMF were obtained from Fisher Scientific. Preloaded Wang resin and OxymaPure were obtained from CEM.

The linear peptide sequences were synthesized via solid-phase peptide synthesis (SPPS) on a LibertyBlue microwave synthesizer (CEM) at 0.1mmol scale on preloaded Wang resin. The complete linear peptide sequence was then coupled by hand to Fmoc-6-aminohexanoic acid (AHX) (3eq), HATU (3 eq), and DIPEA (5eq) for 3h, washed with DMF, then treated with 20% piperidine in DMF for 2x15m to remove Fmoc. The resin was then washed with DMF and swelled in 50/50 DMSO/DMF prior to coupling with biotin (3eq), HATU (eq), and DIPEA (5eq) for 3h, then washed with DMF and DCM prior to total deprotection and cleavage from resin using a cleavage cocktail (92.5:2.5:2.5:2.5 TFA:triisopropylsilane:H_2O:2,2'-(ethylenedioxy)diethanethiol, v/v/v/v) for 3h. The peptide cleavage solution was concentrated *in vacuo* and precipitated in ice-cold diethyl ether, centrifuged to pellet the peptide crude (7000g, 4°C, 10m), and dried under N_2. The peptide crude was resuspended in minimal water and acetonitrile and purified by RP-HPLC on a semi-prep Agilent 1260 Infinity with a linear gradient from 10-45% A->B (A: water with 0.1% TFA, B: ACN with 0.1% TFA) on a Zorbax C18-300SB 5 μm 9.4x250mm column (Agilent), and analyzed via LC/MS-TOF on an Agilent G6230B (Figure S10). Pure peptide fractions were combined and lyophilized.

Palmitoylated and prenylated versions of KRAS4A, HRAS (two palmitoylations), and NRAS C-termini were ordered from Genscript.

DNA library preparation

All protein sequences were padded to a uniform length by adding a (GGGS)n linker at the C terminal of the designs, to avoid the biased amplification of short DNA fragments during PCR reactions. The protein sequences were reversed translated and optimized using DNAworks2.0 with the S. cerevisiae codon frequency table. Homologous to the pETCON plasmid Oligo libraries encoding the designs were ordered from Twist Bioscience. Combinatorial libraries were ordered as IDT (Integrated DNA Technologies) ultramers with the final DNA diversity ranging from 1×10^6 to 1×10^7.

All libraries were amplified using Kapa HiFi Polymerase (Kapa Biosystems) with a qPCR machine (BioRAD CFX96). In detail, the libraries were firstly amplified in a 25 μL reaction, and PCR reaction was terminated when the reaction reached half the maximum yield to avoid over-amplification. The PCR product was loaded to a DNA agarose gel. The band with the expected size was cut out and DNA fragments were extracted using QIAquick kits (Qiagen, Inc.). Then, the DNA product was re-amplified as before to generate enough DNA for yeast transformation. The final PCR product was cleaned up with a QIAquick Clean up kit (Qiagen, Inc.). For the yeast transformation, 2-3 μg of digested modified pETcon vector (pETcon3) and 6 μg of insert were transformed into EBY100 yeast strain using the protocol as described before.

DNA libraries for deep sequencing were prepared using the same PCR protocol, except the first step started from yeast plasmid prepared from 5×10^7 to 1×10^8 cells by Zymoprep (Zymo Research). Illumina adapters and 6-bp pool-specific barcodes were added in the second qPCR step. Gel extraction was used to get the final DNA product for sequencing. All libraries include the native library and different sorting pools were sequenced using Illumina NextSeq/MiSeq sequencing.

For mammalian cell expression, all plasmids use the pcDNA3.1 backbone and were produced by GenScript.

Yeast surface display

S. cerevisiae EBY100 strain cultures were grown in C-Trp-Ura media and induced in SGCAA media following the protocol as described before. Cells were washed with PBSF (PBS with 1% BSA) and labeled with biotinylated target using two labeling methods, with-avidity and without-avidity labeling. For the with-avidity method, the cells were incubated with biotinylated target, together with anti-c-Myc fluorescein isothiocyanate (FITC, Miltenyi Biotech) and streptavidin–phycoerythrin (SAPE, ThermoFisher). The concentration of SAPE in the with-avidity method was used at 1/4 concentration of the biotinylated target. The with-avidity method was used in the first few rounds of screening of the original design to fish out weak binder candidates. For the without-avidity method, the cells were firstly incubated with biotinylated target, washed, secondarily labeled with SAPE and FITC. For these designs, the first two to four rounds of sorts were applied with 1 μM concentration of the Ras C-terminus with biotin at the C-terminal end of the peptide. The remaining subsequent sorts were done with varying concentrations (1 nM - 1 μM) of full length RAS. The final sorting pools of the combinatorial libraries were sequenced using Illumina NextSeq/MiSeq sequencing. All FACS data was analyzed in FlowJo.

Cell transfection and siRNA information

Before transfection, all cells were plated onto sterile poly-D-lysine coated plates or dishes and grown to 50%–70% confluence. All cells were transfected with Lipofectamine LTX. Subsequently, all cells were grown for an additional 1-2 days before experimental testing. All cells underwent serum starvation for 16 hours before downstream assay analysis. Throughout the paper, transfection efficiencies for HEK293T cells are ~70%, HeLa cells are ~10%, and the rest are ~5%. See Table S3 for details of reagents.

siRNAs were selected based on a previous report[5] and are the following sequences: HRAS: CAGAUGGGAUCACAGUAAA, NRAS: GGAGCAGAUUAAGCGAGUA, KRAS: GCCUUGACGAUACAGCUAA.

General procedures for bacterial protein production and purification

The *E. coli* Lemo21(DE3) strain was transformed with a pET29b$^+$ plasmid encoding the synthesized gene of interest. Cells were grown for 24 hours in liquid broth medium supplemented with kanamycin. Cells were inoculated at a 1:50 ml ratio in the Studier TBM-5052 autoinduction medium supplemented with kanamycin, grown at 37°C for 2–4 hours and then grown at 18°C for an additional 18 hours. Cells were collected by centrifugation at 4,000 *g* at 4 °C for 15 min and resuspended in 30 ml lysis buffer (20 mM Tris-HCl, pH 8.0, 300 mM NaCl, 30 mM imidazole, 1 mM PMSF and 0.02 mg ml^{-1} DNase). Cell resuspensions were lysed by sonication for 2.5 min (5 s cycles). Lysates were clarified by centrifugation at 24,000 *g* at 4°C for 20 min and passed through 2-ml Ni-NTA nickel resin pre-equilibrated with wash buffer (20 mM Tris-HCl, pH 8.0, 300 mM NaCl and 30 mM imidazole). The resin was washed twice with 10 column volumes of wash buffer, and then eluted with 3 column volumes of elution buffer (20 mM Tris-HCl, pH 8.0, 300 mM NaCl and 300 mM imidazole). The eluted proteins were concentrated using Ultra-15 Centrifugal Filter Units and further purified by using a Superdex 75 Increase 10/300 GL size exclusion column in TBS (25 mM Tris-HCl, pH 8.0, and 150 mM NaCl). Fractions containing monomeric protein were pooled, concentrated and snap-frozen in liquid nitrogen and stored at −80°C. See Table S3 for details of reagents.

To biotinylate RIBs, an AviTag was added at their C-terminus. Biotinylation of purified RIBs fused with AviTags was performed using the BirA bulk kit according to manufacturer's protocol (Avidity LLC). Briefly, biotinylation reactions (pH 8.0; 1:1 ratio) were performed for 1 hour at 4°C on an orbital shaker and then excess biotinylation reagent was removed using Superdex 200 Increase 10/300 GL (depending on kDa of protein) size exclusion column in TBS (25 mM Tris-HCl, pH 8.0, and 150 mM NaCl).

Please cite this article in press as: Zhang et al., *De novo* design of Ras isoform selective binders, Cell Chemical Biology (2026), https://doi.org/10.1016/j.chembiol.2026.02.008

Biolayer interferometry

Protein–protein interactions were measured by using an Octet RED96 System (ForteBio) using streptavidin-coated biosensors (ForteBio). Each well contained 200 μL of solution, and the assay buffer was HBS-EP+ buffer (GE Healthcare Life Sciences, 10 mM HEPES pH 7.4, 150 mM NaCl, 3 mM EDTA, 0.05% (v/v) surfactant P20) plus 0.5% non-fat dry milk blotting grade blocker (BioRad). The biosensor tips were loaded with analyte peptide or protein at 20 μg mL^{-1} for 300 s (threshold of 0.8 nm response), incubated in HBS-EP+ buffer for 60 s to acquire the baseline measurement, dipped into the solution containing cage and/or key for 1800 s (association step) and dipped into the HBS-EP+ buffer for 1800 s (dissociation steps). The binding data were analyzed with the ForteBio Data Analysis Software version 9.0.0.10.

Immunostaining

All cell lines were seeded onto 24-well glass-bottom plates. After transfection and drug addition, cells were fixed with 4% PFA in 2x PHEM buffer (60 mM PIPES, 50 mM HEPES, 20 mM EGTA, 4 mM $MgCl_2$, 0.25 M sucrose, pH 7.3) for 10 min, permeabilized with 100% methanol for 10 min, washed with PBS 3x, blocked in 1% BSA in PBS for 30 min, incubated with biotinylated RIBs and antibodies for 2 hours at room temperature, washed with PBS 3x, incubated with DAPI and fluorescently labeled reagents (streptavidin and BioTracker) for 1 hour at room temperature and aluminum foil cover. Cells were then washed with PBS 3x and mounted for epifluorescence imaging. All images were analyzed in ImageJ. See Table S3 for details of reagents.

Membrane fractionation

Subcellular protein fractions were prepared using the Thermo Scientific Subcellular Protein Fractionation Kit for Cultured Cells, following the manufacturer's protocol. This method facilitates the sequential separation of cytoplasmic, membrane-associated, nuclear soluble, chromatin-bound, and cytoskeletal proteins from cultured mammalian cells.

Briefly, cell pellets were resuspended in a cytoplasmic extraction buffer, which selectively permeabilizes the plasma membrane to release soluble cytoplasmic proteins and the sample was centrifuged at 500g. The supernatant was treated with a membrane extraction buffer that solubilizes the plasma, mitochondrial, and endoplasmic reticulum/Golgi membranes, leaving nuclear membranes intact and the sample was centrifuged at 3000g. Intact nuclei were recovered by centrifugation, and nuclear soluble proteins were extracted using a nuclear extraction buffer and centrifugation at 5000g. Finally, the insoluble fraction was extracted using a pellet extraction buffer to isolate cytoskeletal proteins and centrifugation at 16000g. Each fraction was collected and stored at -80°C until further analysis.

Immunoblotting and immunoprecipitation

Cells expressing indicated constructs and incubated with indicated drugs were plated, transfected, and labeled as described in figure legends. Cells were then transferred to ice and washed 2x with ice cold DPBS. Cells were then detached from the well by addition of 1x RIPA lysis buffer (50 mM Tris pH 8, 150 mM NaCl, 0.1% SDS, 0.5% sodium deoxycholate, 1% Triton X-100, 1x protease inhibitor cocktail, 1 mM PMSF, 1mM Na_3VO_4, 1% NP-40) and either scraping of cells or rotation on shaker for 30 min at 4°C. Cells were then collected and vortexed for at least 5 s every 10 min for 20 min at 4°C. Cells were then collected and clarified by centrifugation at 13,000g for 10 minutes at 4°C. The supernatant was collected and underwent Pierce BCA assay to quantify total protein amounts.

For immunoblotting, whole cell lysate protein amounts were normalized across samples in the same gel, mixed with 4x loading buffer prior to loading, incubated at 95°C for 5 min and then 4°C for 5 min, and separated on Any kDa SDS-PAGE gels. Proteins separated on SDS-page gels were transferred to nitrocellulose membranes via the TransBlot system (BioRad). The blots were then blocked in 5% milk (w/v) in TBST (Tris-buffered saline, 0.1% Tween 20) for 1 hour at room temperature. Blots were washed with TBST 3x then incubated with indicated primary antibodies or biotinylated RIBs in 1% BSA (w/v) in TBST overnight at 4°C. Blots were then washed with TBST 3x and incubated with LICOR dye-conjugated secondary antibodies (LICOR 680/800 or streptavidin-LICOR 800) and fluorescently labeled streptavidin in 1% BSA (w/v) in TBST for 1 hour at room temperature. The blots were washed with TBST 3x and imaged on an Odyssey IR imager (LICOR). Quantitation of Western blots was performed using ImageJ on raw images. See Table S3 for details of reagents including antibody dilutions.

For immunoprecipitation, streptavidin beads were loaded by three lysis buffer washes before the addition of 1 mg ml^{-1} of biotinylated RIBs at 4°C on an orbital shaker for 3 h. Beads were then washed two times in lysis buffer. Whole-cell lysate protein amounts were normalized across samples and protein samples were added to beads (at least 100 μg per sample) either at room temperature for 1 h for streptavidin beads or at 4°C on an orbital shaker overnight. Beads were then washed two times in lysis buffer and one time in TBS and then mixed with 4× loading buffer. The remaining portion of the protocol was the same as for immunoblotting. Full blots are shown in Figure S11.

Epifluorescence imaging

Cells were washed twice with FluoroBrite DMEM imaging media and subsequently imaged in the same media in the dark at room temperature. Epifluorescence imaging was performed on a Yokogawa CSU-X1 spinning dish confocal microscope with either a Lumencor Celesta light engine with 7 laser lines (408, 445, 473, 518, 545, 635, 750 nm) or a Nikon LUN-F XL laser launch with 4 solid state lasers (405, 488, 561, 640 nm), 40x/0.95 NA objective or 60x/1.4 NA oil immersion objective and a Hamamatsu ORCA-Fusion scientific CMOS camera, both controlled by NIS Elements 5.30 software (Nikon). The following laser and filter combinations

(center/bandwidth in nm) were used: GFP: EX473 EM525/36, RFP: EX545 EM605/52, BFP: EX445 EM525/36. Exposure times were 500ms for all channels, with no EM gain set and no ND filter added. All epifluorescence experiments were subsequently analyzed using Image J. Brightfield images were acquired on the ZOE Fluorescent Cell Imager (BioRad). See Table S3 for details of reagents.

Co-localization analysis

For co-localization analysis, cell images were individually thresholded and underwent Coloc 2 analysis on ImageJ. Mander's coefficient, which ranges from 0 to 1 with 1 being 100% colocalized, is measuring the spatial overlap of one imaging channel with another imaging channel. Pearson's coefficient compares the pixel intensity of one channel with another channel. Pearson's coefficient values can range from -1 to 1 with -1 meaning inversely proportional and 1 meaning same pixel intensities.

MOLM-13 cell line generation and cell growth assays

MOLM-13 KRAS and NRAS mutant cell lines were generated as previously described.[25,26] Briefly, the plasmids pCW57.1 (Addgene 41393), pDONR223 KRAS WT (Addgene 81751), and pDONR223 NRAS WT (Addgene 82151) were used to generate doxycycline-inducible KRAS and NRAS constructs. mCherry was cloned (Addgene 60954) to the N-terminus of KRAS or NRAS on the pCW57.1 backbone and site-directed mutagenesis was performed to generate KRAS and NRAS mutations. MOLM-13 cells (DSMZ) were transduced with lentivirus generated from these constructs and sorted for mCherry positivity after treatment with doxycycline 2 μg/mL. MOLM-13 cells were transfected with plasmids and treated with doxycycline 2 μg/mL (if indicated). 6 hours later, 10 nM AC220 (quizartinib) was added and this addition marks the start of the cell counting (t=0 days). Cell counts were obtained using a Countess 3 automated cell counter (ThermoFisher).

Graphics

All schematics were generated using BioRender.

QUANTIFICATION AND STATISTICAL ANALYSIS

Statistics and reproducibility

No statistical methods were used to predetermine the sample size. No sample was excluded from data analysis, and no blinding was used. All data were assessed for normality. For normally distributed data, pairwise comparisons were performed using unpaired two-tailed Student's t tests, with Welch's correction for unequal variances used as indicated. Comparisons between three or more groups were performed using ordinary one-way or two-way analysis of variance (ANOVA) as indicated. For data that were not normally distributed, pairwise comparisons were performed using the Mann-Whitney U test, and comparisons between multiple groups were performed using the Kruskal-Wallis test. All data shown are reported as mean ± SEM and error bars in figures represent SEM of biological triplicates. All data were analyzed and plotted using GraphPad Prism 8 including non-linear regression fitting.